

Study of $e^+e^- \rightarrow \gamma\phi J/\psi$ from $\sqrt{s} = 4.600$ to 4.951 GeV

The BESIII Collaboration



M. Ablikim¹, M. N. Achasov^{12,b}, P. Adlarson⁷², M. Albrecht⁴, R. Aliberti³³,
 A. Amoroso^{71A,71C}, M. R. An³⁷, Q. An^{68,55}, Y. Bai⁵⁴, O. Bakina³⁴, R. Baldini
 Ferroli^{27A}, I. Balossino^{28A}, Y. Ban^{44,g}, V. Batozskaya^{1,42}, D. Becker³³,
 K. Begzsuren³⁰, N. Berger³³, M. Bertani^{27A}, D. Bettoni^{28A}, F. Bianchi^{71A,71C},
 E. Bianco^{71A,71C}, J. Bloms⁶⁵, A. Bortone^{71A,71C}, I. Boyko³⁴, R. A. Briere⁵,
 A. Brueggemann⁶⁵, H. Cai⁷³, X. Cai^{1,55}, A. Calcaterra^{27A}, G. F. Cao^{1,60}, N. Cao^{1,60},
 S. A. Cetin^{59A}, J. F. Chang^{1,55}, W. L. Chang^{1,60}, G. R. Che⁴¹, G. Chelkov^{34,a},
 C. Chen⁴¹, Chao Chen⁵², G. Chen¹, H. S. Chen^{1,60}, M. L. Chen^{1,55,60}, S. J. Chen⁴⁰,
 S. M. Chen⁵⁸, T. Chen^{1,60}, X. R. Chen^{29,60}, X. T. Chen^{1,60}, Y. B. Chen^{1,55},
 Z. J. Chen^{24,h}, W. S. Cheng^{71C}, S. K. Choi⁵², X. Chu⁴¹, G. Cibinetto^{28A},
 F. Cossio^{71C}, J. J. Cui⁴⁷, H. L. Dai^{1,55}, J. P. Dai⁷⁶, A. Dbeyssi¹⁸, R. E. de Boer⁴,
 D. Dedovich³⁴, Z. Y. Deng¹, A. Denig³³, I. Denysenko³⁴, M. Destefanis^{71A,71C},
 F. De Mori^{71A,71C}, Y. Ding³⁸, Y. Ding³², J. Dong^{1,55}, L. Y. Dong^{1,60},
 M. Y. Dong^{1,55,60}, X. Dong⁷³, S. X. Du⁷⁸, Z. H. Duan⁴⁰, P. Egorov^{34,a}, Y. L. Fan⁷³,
 J. Fang^{1,55}, S. S. Fang^{1,60}, W. X. Fang¹, Y. Fang¹, R. Farinelli^{28A}, L. Fava^{71B,71C},
 F. Feldbauer⁴, G. Felici^{27A}, C. Q. Feng^{68,55}, J. H. Feng⁵⁶, K. Fischer⁶⁶, M. Fritsch⁴,
 C. Fritsch⁶⁵, C. D. Fu¹, H. Gao⁶⁰, Y. N. Gao^{44,g}, Yang Gao^{68,55}, S. Garbolino^{71C},
 I. Garzia^{28A,28B}, P. T. Ge⁷³, Z. W. Ge⁴⁰, C. Geng⁵⁶, E. M. Gersabeck⁶⁴, A. Gilman⁶⁶,
 K. Goetzen¹³, L. Gong³⁸, W. X. Gong^{1,55}, W. Gradl³³, M. Greco^{71A,71C}, L. M. Gu⁴⁰,
 M. H. Gu^{1,55}, Y. T. Gu¹⁵, C. Y. Guan^{1,60}, A. Q. Guo^{29,60}, L. B. Guo³⁹, R. P. Guo⁴⁶,
 Y. P. Guo^{11,f}, A. Guskov^{34,a}, W. Y. Han³⁷, X. Q. Hao¹⁹, F. A. Harris⁶², K. K. He⁵²,
 K. L. He^{1,60}, F. H. Heinsius⁴, C. H. Heinz³³, Y. K. Heng^{1,55,60}, C. Herold⁵⁷,
 G. Y. Hou^{1,60}, Y. R. Hou⁶⁰, Z. L. Hou¹, H. M. Hu^{1,60}, J. F. Hu^{53,i}, T. Hu^{1,55,60},
 Y. Hu¹, G. S. Huang^{68,55}, K. X. Huang⁵⁶, L. Q. Huang^{29,60}, X. T. Huang⁴⁷,
 Y. P. Huang¹, Z. Huang^{44,g}, T. Hussain⁷⁰, N. Hüsken^{26,33}, W. Imoehl²⁶, M. Irshad^{68,55},
 J. Jackson²⁶, S. Jaeger⁴, S. Janchiv³⁰, E. Jang⁵², J. H. Jeong⁵², Q. Ji¹, Q. P. Ji¹⁹,
 X. B. Ji^{1,60}, X. L. Ji^{1,55}, Y. Y. Ji⁴⁷, Z. K. Jia^{68,55}, P. C. Jiang^{44,g}, S. S. Jiang³⁷,
 X. S. Jiang^{1,55,60}, Y. Jiang⁶⁰, J. B. Jiao⁴⁷, Z. Jiao²², S. Jin⁴⁰, Y. Jin⁶³, M. Q. Jing^{1,60},
 T. Johansson⁷², S. Kabana³¹, N. Kalantar-Nayestanaki⁶¹, X. L. Kang⁹, X. S. Kang³⁸,

R. Kappert⁶¹, M. Kavatsyuk⁶¹, B. C. Ke⁷⁸, I. K. Keshk⁴, A. Khoukaz⁶⁵, R. Kiuchi¹,
 R. Kliemt¹³, L. Koch³⁵, O. B. Kolcu^{59A}, B. Kopf⁴, M. Kuemmel⁴, M. Kuessner⁴,
 A. Kupsc^{42,72}, W. Kühn³⁵, J. J. Lane⁶⁴, J. S. Lange³⁵, P. Larin¹⁸, A. Lavania²⁵,
 L. Lavezzi^{71A,71C}, T. T. Lei^{68,k}, Z. H. Lei^{68,55}, H. Leithoff³³, M. Lellmann³³,
 T. Lenz³³, C. Li⁴⁵, C. Li⁴¹, C. H. Li³⁷, Cheng Li^{68,55}, D. M. Li⁷⁸, F. Li^{1,55}, G. Li¹,
 H. Li^{68,55}, H. B. Li^{1,60}, H. J. Li¹⁹, H. N. Li^{53,i}, Hui Li⁴¹, J. Q. Li⁴, J. S. Li⁵⁶,
 J. W. Li⁴⁷, Ke Li¹, L. J. Li^{1,60}, L. K. Li¹, Lei Li³, M. H. Li⁴¹, P. R. Li^{36,j,k}, S. X. Li¹¹,
 S. Y. Li⁵⁸, T. Li⁴⁷, W. D. Li^{1,60}, W. G. Li¹, X. H. Li^{68,55}, X. L. Li⁴⁷, Xiaoyu Li^{1,60},
 Y. G. Li^{44,g}, Z. X. Li¹⁵, Z. Y. Li⁵⁶, C. Liang⁴⁰, H. Liang³², H. Liang^{1,60}, H. Liang^{68,55},
 Y. F. Liang⁵¹, Y. T. Liang^{29,60}, G. R. Liao¹⁴, L. Z. Liao⁴⁷, J. Libby²⁵, A. Limphirat⁵⁷,
 C. X. Lin⁵⁶, D. X. Lin^{29,60}, T. Lin¹, B. J. Liu¹, C. Liu³², C. X. Liu¹, D. Liu^{18,68},
 F. H. Liu⁵⁰, Fang Liu¹, Feng Liu⁶, G. M. Liu^{53,i}, H. Liu^{36,j,k}, H. B. Liu¹⁵,
 H. M. Liu^{1,60}, Huanhuan Liu¹, Huihui Liu²⁰, J. B. Liu^{68,55}, J. L. Liu⁶⁹, J. Y. Liu^{1,60},
 K. Liu¹, K. Y. Liu³⁸, Ke Liu²¹, L. Liu^{68,55}, Lu Liu⁴¹, M. H. Liu^{11,f}, P. L. Liu¹, Q. Liu⁶⁰,
 S. B. Liu^{68,55}, T. Liu^{11,f}, W. K. Liu⁴¹, W. M. Liu^{68,55}, X. Liu^{36,j,k}, Y. Liu^{36,j,k},
 Y. B. Liu⁴¹, Z. A. Liu^{1,55,60}, Z. Q. Liu⁴⁷, X. C. Lou^{1,55,60}, F. X. Lu⁵⁶, H. J. Lu²²,
 J. G. Lu^{1,55}, X. L. Lu¹, Y. Lu⁷, Y. P. Lu^{1,55}, Z. H. Lu^{1,60}, C. L. Luo³⁹, M. X. Luo⁷⁷,
 T. Luo^{11,f}, X. L. Luo^{1,55}, X. R. Lyu⁶⁰, Y. F. Lyu⁴¹, F. C. Ma³⁸, H. L. Ma¹,
 L. L. Ma⁴⁷, M. M. Ma^{1,60}, Q. M. Ma¹, R. Q. Ma^{1,60}, R. T. Ma⁶⁰, X. Y. Ma^{1,55},
 Y. Ma^{44,g}, F. E. Maas¹⁸, M. Maggiora^{71A,71C}, S. Maldaner⁴, S. Malde⁶⁶,
 Q. A. Malik⁷⁰, A. Mangoni^{27B}, Y. J. Mao^{44,g}, Z. P. Mao¹, S. Marcello^{71A,71C},
 Z. X. Meng⁶³, J. G. Messchendorp^{13,61}, G. Mezzadri^{28A}, H. Miao^{1,60}, T. J. Min⁴⁰,
 R. E. Mitchell²⁶, X. H. Mo^{1,55,60}, N. Yu. Muchnoi^{12,b}, Y. Nefedov³⁴, F. Nerling^{18,d},
 I. B. Nikolaev^{12,b}, Z. Ning^{1,55}, S. Nisar^{10,l}, Y. Niu⁴⁷, S. L. Olsen⁶⁰, Q. Ouyang^{1,55,60},
 S. Pacetti^{27B,27C}, X. Pan⁵², Y. Pan⁵⁴, A. Pathak³², Y. P. Pei^{68,55}, M. Pelizaeus⁴,
 H. P. Peng^{68,55}, K. Peters^{13,d}, J. L. Ping³⁹, R. G. Ping^{1,60}, S. Plura³³, S. Pogodin³⁴,
 V. Prasad^{68,55}, F. Z. Qi¹, H. Qi^{68,55}, H. R. Qi⁵⁸, M. Qi⁴⁰, T. Y. Qi^{11,f}, S. Qian^{1,55},
 W. B. Qian⁶⁰, Z. Qian⁵⁶, C. F. Qiao⁶⁰, J. J. Qin⁶⁹, L. Q. Qin¹⁴, X. P. Qin^{11,f},
 X. S. Qin⁴⁷, Z. H. Qin^{1,55}, J. F. Qiu¹, S. Q. Qu⁵⁸, K. H. Rashid⁷⁰, C. F. Redmer³³,
 K. J. Ren³⁷, A. Rivetti^{71C}, V. Rodin⁶¹, M. Rolo^{71C}, G. Rong^{1,60}, Ch. Rosner¹⁸,
 S. N. Ruan⁴¹, A. Sarantsev^{34,c}, Y. Schelhaas³³, C. Schnier⁴, K. Schoenning⁷²,
 M. Scodeggio^{28A,28B}, K. Y. Shan^{11,f}, W. Shan²³, X. Y. Shan^{68,55}, J. F. Shangguan⁵²,
 L. G. Shao^{1,60}, M. Shao^{68,55}, C. P. Shen^{11,f}, H. F. Shen^{1,60}, W. H. Shen⁶⁰,
 X. Y. Shen^{1,60}, B. A. Shi⁶⁰, H. C. Shi^{68,55}, J. Y. Shi¹, q. q. Shi⁵², R. S. Shi^{1,60},
 X. Shi^{1,55}, J. J. Song¹⁹, W. M. Song^{32,1}, Y. X. Song^{44,g}, S. Sosio^{71A,71C},
 S. Spataro^{71A,71C}, F. Stieler³³, P. P. Su⁵², Y. J. Su⁶⁰, G. X. Sun¹, H. Sun⁶⁰,
 H. K. Sun¹, J. F. Sun¹⁹, L. Sun⁷³, S. S. Sun^{1,60}, T. Sun^{1,60}, W. Y. Sun³²,
 Y. J. Sun^{68,55}, Y. Z. Sun¹, Z. T. Sun⁴⁷, Y. X. Tan^{68,55}, C. J. Tang⁵¹, G. Y. Tang¹,
 J. Tang⁵⁶, L. Y. Tao⁶⁹, Q. T. Tao^{24,h}, M. Tat⁶⁶, J. X. Teng^{68,55}, V. Thoren⁷²,
 W. H. Tian⁴⁹, Y. Tian^{29,60}, I. Uman^{59B}, B. Wang^{68,55}, B. Wang¹, B. L. Wang⁶⁰,
 C. W. Wang⁴⁰, D. Y. Wang^{44,g}, F. Wang⁶⁹, H. J. Wang^{36,j,k}, H. P. Wang^{1,60},
 K. Wang^{1,55}, L. L. Wang¹, M. Wang⁴⁷, Meng Wang^{1,60}, S. Wang¹⁴, S. Wang^{11,f}, T.
 Wang^{11,f}, T. J. Wang⁴¹, W. Wang⁵⁶, W. H. Wang⁷³, W. P. Wang^{68,55}, X. Wang^{44,g},

X. F. Wang^{36,j,k}, X. L. Wang^{11,f}, Y. Wang⁵⁸, Y. D. Wang⁴³, Y. F. Wang^{1,55,60},
Y. H. Wang⁴⁵, Y. Q. Wang¹, Yaqian Wang^{17,1}, Z. Wang^{1,55}, Z. Y. Wang^{1,60},
Ziyi Wang⁶⁰, D. H. Wei¹⁴, F. Weidner⁶⁵, S. P. Wen¹, D. J. White⁶⁴, U. Wiedner⁴,
G. Wilkinson⁶⁶, M. Wolke⁷², L. Wollenberg⁴, J. F. Wu^{1,60}, L. H. Wu¹, L. J. Wu^{1,60},
X. Wu^{11,f}, X. H. Wu³², Y. Wu⁶⁸, Y. J. Wu²⁹, Z. Wu^{1,55}, L. Xia^{68,55}, T. Xiang^{44,g},
D. Xiao^{36,j,k}, G. Y. Xiao⁴⁰, H. Xiao^{11,f}, S. Y. Xiao¹, Y. L. Xiao^{11,f}, Z. J. Xiao³⁹,
C. Xie⁴⁰, X. H. Xie^{44,g}, Y. Xie⁴⁷, Y. G. Xie^{1,55}, Y. H. Xie⁶, Z. P. Xie^{68,55},
T. Y. Xing^{1,60}, C. F. Xu^{1,60}, C. J. Xu⁵⁶, G. F. Xu¹, H. Y. Xu⁶³, Q. J. Xu¹⁶,
X. P. Xu⁵², Y. C. Xu⁷⁵, Z. P. Xu⁴⁰, F. Yan^{11,f}, L. Yan^{11,f}, W. B. Yan^{68,55},
W. C. Yan⁷⁸, H. J. Yang^{48,e}, H. L. Yang³², H. X. Yang¹, Tao Yang¹, Y. F. Yang⁴¹,
Y. X. Yang^{1,60}, Yifan Yang^{1,60}, M. Ye^{1,55}, M. H. Ye⁸, J. H. Yin¹, Z. Y. You⁵⁶,
B. X. Yu^{1,55,60}, C. X. Yu⁴¹, G. Yu^{1,60}, T. Yu⁶⁹, X. D. Yu^{44,g}, C. Z. Yuan^{1,60}, L. Yuan²,
S. C. Yuan¹, X. Q. Yuan¹, Y. Yuan^{1,60}, Z. Y. Yuan⁵⁶, C. X. Yue³⁷, A. A. Zafar⁷⁰,
F. R. Zeng⁴⁷, X. Zeng⁶, Y. Zeng^{24,h}, X. Y. Zhai³², Y. H. Zhan⁵⁶, A. Q. Zhang^{1,60},
B. L. Zhang^{1,60}, B. X. Zhang¹, D. H. Zhang⁴¹, G. Y. Zhang¹⁹, H. Zhang⁶⁸,
H. H. Zhang⁵⁶, H. H. Zhang³², H. Q. Zhang^{1,55,60}, H. Y. Zhang^{1,55}, J. J. Zhang⁴⁹,
J. L. Zhang⁷⁴, J. Q. Zhang³⁹, J. W. Zhang^{1,55,60}, J. X. Zhang^{36,j,k}, J. Y. Zhang¹,
J. Z. Zhang^{1,60}, Jianyu Zhang^{1,60}, Jiawei Zhang^{1,60}, L. M. Zhang⁵⁸, L. Q. Zhang⁵⁶,
Lei Zhang⁴⁰, P. Zhang¹, Q. Y. Zhang^{37,78}, Shuihan Zhang^{1,60}, Shulei Zhang^{24,h},
X. D. Zhang⁴³, X. M. Zhang¹, X. Y. Zhang⁴⁷, X. Y. Zhang⁵², Y. Zhang⁶⁶, Y.
T. Zhang⁷⁸, Y. H. Zhang^{1,55}, Yan Zhang^{68,55}, Yao Zhang¹, Z. H. Zhang¹,
Z. L. Zhang³², Z. Y. Zhang⁷³, Z. Y. Zhang⁴¹, G. Zhao¹, J. Zhao³⁷, J. Y. Zhao^{1,60},
J. Z. Zhao^{1,55}, Lei Zhao^{68,55}, Ling Zhao¹, M. G. Zhao⁴¹, S. J. Zhao⁷⁸, Y. B. Zhao^{1,55},
Y. X. Zhao^{29,60}, Z. G. Zhao^{68,55}, A. Zhemchugov^{34,a}, B. Zheng⁶⁹, J. P. Zheng^{1,55},
Y. H. Zheng⁶⁰, B. Zhong³⁹, C. Zhong⁶⁹, X. Zhong⁵⁶, H. Zhou⁴⁷, L. P. Zhou^{1,60},
X. Zhou⁷³, X. K. Zhou⁶⁰, X. R. Zhou^{68,55}, X. Y. Zhou³⁷, Y. Z. Zhou^{11,f}, J. Zhu⁴¹,
K. Zhu¹, K. J. Zhu^{1,55,60}, L. X. Zhu⁶⁰, S. H. Zhu⁶⁷, S. Q. Zhu⁴⁰, T. J. Zhu⁷⁴,
W. J. Zhu^{11,f}, Y. C. Zhu^{68,55}, Z. A. Zhu^{1,60}, J. H. Zou¹, J. Zu^{68,55}

(BESIII Collaboration)

¹ *Institute of High Energy Physics, Beijing 100049, People's Republic of China*

² *Beihang University, Beijing 100191, People's Republic of China*

³ *Beijing Institute of Petrochemical Technology, Beijing 102617, People's Republic of China*

⁴ *Bochum Ruhr-University, D-44780 Bochum, Germany*

⁵ *Carnegie Mellon University, Pittsburgh, Pennsylvania 15213, USA*

⁶ *Central China Normal University, Wuhan 430079, People's Republic of China*

⁷ *Central South University, Changsha 410083, People's Republic of China*

⁸ *China Center of Advanced Science and Technology, Beijing 100190, People's Republic of China*

⁹ *China University of Geosciences, Wuhan 430074, People's Republic of China*

¹⁰ *COMSATS University Islamabad, Lahore Campus, Defence Road, Off Raiwind Road, 54000 Lahore, Pakistan*

- 11 *Fudan University, Shanghai 200433, People's Republic of China*
- 12 *G.I. Budker Institute of Nuclear Physics SB RAS (BINP), Novosibirsk 630090, Russia*
- 13 *GSI Helmholtzcentre for Heavy Ion Research GmbH, D-64291 Darmstadt, Germany*
- 14 *Guangxi Normal University, Guilin 541004, People's Republic of China*
- 15 *Guangxi University, Nanning 530004, People's Republic of China*
- 16 *Hangzhou Normal University, Hangzhou 310036, People's Republic of China*
- 17 *Hebei University, Baoding 071002, People's Republic of China*
- 18 *Helmholtz Institute Mainz, Staudinger Weg 18, D-55099 Mainz, Germany*
- 19 *Henan Normal University, Xinxiang 453007, People's Republic of China*
- 20 *Henan University of Science and Technology, Luoyang 471003, People's Republic of China*
- 21 *Henan University of Technology, Zhengzhou 450001, People's Republic of China*
- 22 *Huangshan College, Huangshan 245000, People's Republic of China*
- 23 *Hunan Normal University, Changsha 410081, People's Republic of China*
- 24 *Hunan University, Changsha 410082, People's Republic of China*
- 25 *Indian Institute of Technology Madras, Chennai 600036, India*
- 26 *Indiana University, Bloomington, Indiana 47405, USA*
- 27 *INFN Laboratori Nazionali di Frascati , (A)INFN Laboratori Nazionali di Frascati, I-00044, Frascati, Italy; (B)INFN Sezione di Perugia, I-06100, Perugia, Italy; (C)University of Perugia, I-06100, Perugia, Italy*
- 28 *INFN Sezione di Ferrara, (A)INFN Sezione di Ferrara, I-44122, Ferrara, Italy; (B)University of Ferrara, I-44122, Ferrara, Italy*
- 29 *Institute of Modern Physics, Lanzhou 730000, People's Republic of China*
- 30 *Institute of Physics and Technology, Peace Avenue 54B, Ulaanbaatar 13330, Mongolia*
- 31 *Instituto de Alta Investigación, Universidad de Tarapacá, Casilla 7D, Arica, Chile*
- 32 *Jilin University, Changchun 130012, People's Republic of China*
- 33 *Johannes Gutenberg University of Mainz, Johann-Joachim-Becher-Weg 45, D-55099 Mainz, Germany*
- 34 *Joint Institute for Nuclear Research, 141980 Dubna, Moscow region, Russia*
- 35 *Justus-Liebig-Universitaet Giessen, II. Physikalisches Institut, Heinrich-Buff-Ring 16, D-35392 Giessen, Germany*
- 36 *Lanzhou University, Lanzhou 730000, People's Republic of China*
- 37 *Liaoning Normal University, Dalian 116029, People's Republic of China*
- 38 *Liaoning University, Shenyang 110036, People's Republic of China*
- 39 *Nanjing Normal University, Nanjing 210023, People's Republic of China*
- 40 *Nanjing University, Nanjing 210093, People's Republic of China*
- 41 *Nankai University, Tianjin 300071, People's Republic of China*
- 42 *National Centre for Nuclear Research, Warsaw 02-093, Poland*
- 43 *North China Electric Power University, Beijing 102206, People's Republic of China*
- 44 *Peking University, Beijing 100871, People's Republic of China*
- 45 *Qufu Normal University, Qufu 273165, People's Republic of China*
- 46 *Shandong Normal University, Jinan 250014, People's Republic of China*
- 47 *Shandong University, Jinan 250100, People's Republic of China*

- ⁴⁸ *Shanghai Jiao Tong University, Shanghai 200240, People's Republic of China*
- ⁴⁹ *Shanxi Normal University, Linfen 041004, People's Republic of China*
- ⁵⁰ *Shanxi University, Taiyuan 030006, People's Republic of China*
- ⁵¹ *Sichuan University, Chengdu 610064, People's Republic of China*
- ⁵² *Soochow University, Suzhou 215006, People's Republic of China*
- ⁵³ *South China Normal University, Guangzhou 510006, People's Republic of China*
- ⁵⁴ *Southeast University, Nanjing 211100, People's Republic of China*
- ⁵⁵ *State Key Laboratory of Particle Detection and Electronics, Beijing 100049, Hefei 230026, People's Republic of China*
- ⁵⁶ *Sun Yat-Sen University, Guangzhou 510275, People's Republic of China*
- ⁵⁷ *Suranaree University of Technology, University Avenue 111, Nakhon Ratchasima 30000, Thailand*
- ⁵⁸ *Tsinghua University, Beijing 100084, People's Republic of China*
- ⁵⁹ *Turkish Accelerator Center Particle Factory Group, (A)Istinye University, 34010, Istanbul, Turkey; (B)Near East University, Nicosia, North Cyprus, Mersin 10, Turkey*
- ⁶⁰ *University of Chinese Academy of Sciences, Beijing 100049, People's Republic of China*
- ⁶¹ *University of Groningen, NL-9747 AA Groningen, The Netherlands*
- ⁶² *University of Hawaii, Honolulu, Hawaii 96822, USA*
- ⁶³ *University of Jinan, Jinan 250022, People's Republic of China*
- ⁶⁴ *University of Manchester, Oxford Road, Manchester, M13 9PL, United Kingdom*
- ⁶⁵ *University of Muenster, Wilhelm-Klemm-Strasse 9, 48149 Muenster, Germany*
- ⁶⁶ *University of Oxford, Keble Road, Oxford OX13RH, United Kingdom*
- ⁶⁷ *University of Science and Technology Liaoning, Anshan 114051, People's Republic of China*
- ⁶⁸ *University of Science and Technology of China, Hefei 230026, People's Republic of China*
- ⁶⁹ *University of South China, Hengyang 421001, People's Republic of China*
- ⁷⁰ *University of the Punjab, Lahore-54590, Pakistan*
- ⁷¹ *University of Turin and INFN, (A)University of Turin, I-10125, Turin, Italy; (B)University of Eastern Piedmont, I-15121, Alessandria, Italy; (C)INFN, I-10125, Turin, Italy*
- ⁷² *Uppsala University, Box 516, SE-75120 Uppsala, Sweden*
- ⁷³ *Wuhan University, Wuhan 430072, People's Republic of China*
- ⁷⁴ *Xinyang Normal University, Xinyang 464000, People's Republic of China*
- ⁷⁵ *Yantai University, Yantai 264005, People's Republic of China*
- ⁷⁶ *Yunnan University, Kunming 650500, People's Republic of China*
- ⁷⁷ *Zhejiang University, Hangzhou 310027, People's Republic of China*
- ⁷⁸ *Zhengzhou University, Zhengzhou 450001, People's Republic of China*
- ^a *Also at the Moscow Institute of Physics and Technology, Moscow 141700, Russia*
- ^b *Also at the Novosibirsk State University, Novosibirsk, 630090, Russia*
- ^c *Also at the NRC "Kurchatov Institute", PNPI, 188300, Gatchina, Russia*
- ^d *Also at Goethe University Frankfurt, 60323 Frankfurt am Main, Germany*

^e Also at Key Laboratory for Particle Physics, Astrophysics and Cosmology, Ministry of Education; Shanghai Key Laboratory for Particle Physics and Cosmology; Institute of Nuclear and Particle Physics, Shanghai 200240, People's Republic of China

^f Also at Key Laboratory of Nuclear Physics and Ion-beam Application (MOE) and Institute of Modern Physics, Fudan University, Shanghai 200443, People's Republic of China

^g Also at State Key Laboratory of Nuclear Physics and Technology, Peking University, Beijing 100871, People's Republic of China

^h Also at School of Physics and Electronics, Hunan University, Changsha 410082, China

ⁱ Also at Guangdong Provincial Key Laboratory of Nuclear Science, Institute of Quantum Matter, South China Normal University, Guangzhou 510006, China

^j Also at Frontiers Science Center for Rare Isotopes, Lanzhou University, Lanzhou 730000, People's Republic of China

^k Also at Lanzhou Center for Theoretical Physics, Lanzhou University, Lanzhou 730000, People's Republic of China

^l Also at the Department of Mathematical Sciences, IBA, Karachi , Pakistan

E-mail: besiii-publications@ihep.ac.cn

ABSTRACT: Using data samples with an integrated luminosity of 6.4 fb^{-1} collected by the BESIII detector operating at the BEPCII storage ring, the process of $e^+e^- \rightarrow \gamma\phi J/\psi$ is studied. The processes of $e^+e^- \rightarrow \phi\chi_{c1,c2}$, $\chi_{c1,c2} \rightarrow \gamma J/\psi$ are observed with a significance of more than 10σ . The \sqrt{s} -dependent cross section of $e^+e^- \rightarrow \phi\chi_{c1,c2}$ is measured between 4.600 and 4.951 GeV, and evidence of a resonance structure is found for the first time in the $\phi\chi_{c2}$ process. We also search for the processes of $e^+e^- \rightarrow \gamma X(4140)$, $\gamma X(4274)$ and $\gamma X(4500)$ via the $\gamma\phi J/\psi$ final state, but no obvious structures are found. The upper limits on the production cross section times the branching fraction for these processes at the 90% confidence level are reported.

Contents

1	Introduction	1
2	BESIII detector and MC sample	3
3	Study of $e^+e^- \rightarrow \phi\chi_{c1,c2}$ with $\chi_{c1,c2} \rightarrow \gamma J/\psi$	4
3.1	Event Selection	4
3.1.1	3-track events with $\phi \rightarrow K^+K^-$	4
3.1.2	4-track events with $\phi \rightarrow K^+K^-$	6
3.1.3	Events with $\phi \rightarrow K_S^0 K_L^0$	7
3.2	Cross section measurement	9
3.3	Systematic uncertainty	15
3.3.1	Systematic uncertainty for cross section measurement	15
3.3.2	Systematic uncertainties for the resonance parameters	17
4	Study of $e^+e^- \rightarrow \gamma X$ with $X \rightarrow \phi J/\psi$	18
4.1	Upper limit of $e^+e^- \rightarrow \gamma X$ cross section	19
4.2	Systematic uncertainty	22
5	Summary	22
A	Fit result for $M(\gamma J/\psi)$	28
B	Systematic uncertainty in cross section measurement	29

1 Introduction

In the past decades, several charmonium-like states with $J^{PC} = 1^{--}$ have been discovered, such as the $Y(4260)$ [1–3], $Y(4360)$ [4, 5] and $Y(4660)$ [5–8]. The potential model predicts five vector charmonium states in the mass region between 4.0 and 4.7 GeV/ c^2 , namely $3S$, $2D$, $4S$, $3D$, and $5S$ [9]. The first three states have been identified with the $\psi(4040)$, $\psi(4160)$ and $\psi(4415)$ [10]. Together with the three observed Y -states, we have at least six 1^{--} states in this mass region. In addition, the masses of the undiscovered $3D$ and $5S$ states are expected to be higher than 4.4 GeV/ c^2 , which leaves no room for $Y(4260)$ and $Y(4360)$ in the charmonium spectrum. Unlike the conventional 1^{--} charmonium states which predominantly decay to open charm final states ($D^{(*)}\bar{D}^{(*)}$), the Y -states are found to usually couple with hidden-charm final states [1–5]. Considering these unusual properties, the Y -states are widely regarded as good candidates for unconventional hadron states, such as hybrids, tetraquarks, or meson molecules [11, 12].

At present, the inner structure of these Y -states remains unclear. Experimentally, the e^+e^- annihilation process is one of the most effective ways to probe the nature of Y -states. The $Y(4660)$ resonance was first observed by the Belle Collaboration in $e^+e^- \rightarrow \pi^+\pi^-\psi(3686)$ process via initial-state-radiation (ISR) [5], and subsequently confirmed by the BaBar [6] and BESIII Collaborations [8] in the same process. In the $Y(4660) \rightarrow \pi^+\pi^-\psi(3686)$ decay, the $\pi^+\pi^-$ system is found to be dominated by a $f_0(980)$ which has a significant $s\bar{s}$ component. Recently, the Belle experiment reported the first $Y(4626)$ resonance coupling to the $D_s^+D_{s1}^-(2536) + \text{c.c.}$ meson pair with a significance of 5.9σ [13]. Belle also reported evidence (3.4σ) for a resonance with mass and width consistent with $Y(4626)$ in the $D_s^+D_{s2}^{*-}(2573) + \text{c.c.}$ process [14]. It is not clear whether $Y(4660)$ and $Y(4626)$ correspond to the same resonance or not. The observation of the $Y(4660)$ state coupling to $f_0(980)\psi(3686)$ and the $Y(4626)$ state coupling to the charmed-antistrange and anticharmed-strange meson pair may indicate that $Y(4660)/Y(4626)$ have $c\bar{c}s\bar{s}$ components [15–17]. In such a case, the $Y(4660)/Y(4626)$ may also decay to the final states of $\phi\chi_{c1}$ or $\phi\chi_{c2}$. The BESIII experiment has measured the cross section of $e^+e^- \rightarrow \phi\chi_{c1,c2}$ at 4.600 GeV [18], and significant $\chi_{c1,c2}$ signals were found. With the data taken at center-of-mass (c.m.) energies up to $\sqrt{s} = 4.951$ GeV at BESIII, which fully covers the $Y(4626)$ and $Y(4660)$ mass region, we are able to measure the cross section line shape of $e^+e^- \rightarrow \phi\chi_{c1,c2}$. The measurements may shed light on the inner structure of the $Y(4660)/Y(4626)$ states and help us understand their nature.

In addition to the Y -states, the non-vector X -states in the $\phi J/\psi$ system also attract much interest. A narrow ($\Gamma = 11.7$ MeV) near-threshold peak around 4143 MeV/ c^2 in the $\phi J/\psi$ mass spectrum was first reported by the CDF Collaboration in the $B^+ \rightarrow \phi J/\psi K^+$ process with 3.8σ evidence (labeled as $X(4140)$) [19]. From the potential model, charmonium states within this mass region are expected to have much larger widths due to the open charm decay channels [11]. The $X(4140)$ is therefore suggested to be a candidate of an exotic state. An updated analysis by the CDF Collaboration in 2011 [20] not only confirmed the existence of $X(4140)$ with a 5σ observation, but also reported evidence (3.1σ) of a new narrow peak near 4274 MeV/ c^2 in the $\phi J/\psi$ spectrum. Subsequent measurements were also carried out by the Belle [21], LHCb [22–25], CMS [26], D0 [27, 28], BaBar [29] and BESIII experiments [18, 30]. Belle [21], BaBar [29] and BESIII [18, 30] found no evidence for the $X(4140)$.

The LHCb Collaboration studied the $B^+ \rightarrow \phi J/\psi K^+$ process with 0.37 fb^{-1} of data, and no evidence of resonance structures was found in the $\phi J/\psi$ system [22]. Later, with the full Run1 data (3 fb^{-1}), an updated analysis was performed by the LHCb Collaboration with an amplitude analysis [23, 24]. A near-threshold structure with mass $4146.5 \pm 4.5_{-2.8}^{+4.6}$ MeV/ c^2 and width $83 \pm 21_{-14}^{+21}$ MeV was reported. In addition, they also reported the existence of $X(4274)$, $X(4500)$ and $X(4700)$ in the $\phi J/\psi$ system with significance more than 5σ . Most recently, with the Run1 and Run2 datasets (9 fb^{-1}), LHCb improved their amplitude analysis of $B^+ \rightarrow \phi J/\psi K^+$ with a new model, and a total of seven structures have been observed in the $\phi J/\psi$ system [25]. The abundant structures observed are candidates for exotic hadrons containing $c\bar{c}s\bar{s}$ [31–40], and provide new insight to exotic hadron spectroscopy. At BESIII, it is possible to search for the $\phi J/\psi$ structures,

such as the $X(4140)$, $X(4274)$ and $X(4500)$, through the $e^+e^- \rightarrow \gamma\phi J/\psi$ process.

In this article, we present a study of the $e^+e^- \rightarrow \gamma\phi J/\psi$ process with 6.4 fb^{-1} of data taken at e^+e^- c.m. energies from 4.600 to 4.951 GeV [41–43]. The \sqrt{s} -dependent cross section of $e^+e^- \rightarrow \phi\chi_{c1,c2}$ is measured and possible vector resonances are investigated. The $\chi_{c1,c2}$ resonances are reconstructed with the $\gamma J/\psi$ and $J/\psi \rightarrow \ell^+\ell^-$ ($\ell = e, \mu$) decays. We also search for the possible X -state in the $e^+e^- \rightarrow \gamma X, X \rightarrow \phi J/\psi$ process. To increase the number of candidates, both $\phi \rightarrow K^+K^-$ and $\phi \rightarrow K_S^0 K_L^0$ modes are used to reconstruct ϕ .

2 BESIII detector and MC sample

The BESIII detector [44] records symmetric e^+e^- collisions provided by the BEPCII storage ring [45], which operates with a peak luminosity of $1 \times 10^{33} \text{ cm}^{-2}\text{s}^{-1}$ at e^+e^- center-of-mass energy 3.77 GeV. BESIII has collected large data samples between 2.0 and 4.951 GeV [46]. The cylindrical core of the BESIII detector covers 93% of the full solid angle and consists of a helium-based multilayer drift chamber (MDC), a plastic scintillator time-of-flight system (TOF), and a CsI(Tl) electromagnetic calorimeter (EMC), which are all enclosed in a superconducting solenoidal magnet providing a 1.0 T magnetic field. The solenoid is supported by an octagonal flux-return yoke with resistive plate counter muon chamber (MUC) system interleaved with steel. The charged-particle momentum resolution at 1 GeV/ c is 0.5%, and the dE/dx resolution is 6% for electrons from Bhabha scattering. The EMC measures photon energies with a resolution of 2.5% (5%) at 1 GeV in the barrel (end cap) region. The time resolution in the TOF barrel region is 68 ps, while that in the end cap region was 110 ps. The end cap TOF system was upgraded in 2015 using multi-gap resistive plate chamber technology, providing a time resolution of 60 ps [47]. All the data sets with $\sqrt{s} > 4.600$ GeV are taken with the new end cap TOF system.

Simulated samples produced with a GEANT4-based [48] Monte Carlo (MC) software, which includes the geometric description of the BESIII detector and the detector response, are used to determine detection efficiencies and to estimate backgrounds. The signal MC samples of $e^+e^- \rightarrow \phi\chi_{c1,c2} \rightarrow \gamma\phi J/\psi$ and $e^+e^- \rightarrow \gamma X \rightarrow \gamma\phi J/\psi$ are simulated at each c.m. energy point corresponding to the luminosity of data, with $\phi \rightarrow K^+K^-, K_S^0 K_L^0$ and $J/\psi \rightarrow e^+e^-, \mu^+\mu^-$ being simulated according to the branching fractions taken from the Particle Data Group (PDG) [10]. The inclusive MC sample includes the production of open charm processes, the ISR production of vector charmonium(-like) states, and the continuum processes simulated with KKMC [49]. The simulation models the beam energy spread and ISR in the e^+e^- annihilations with the generator KKMC [49]. The known decay modes of charmed hadrons are modelled with EVTGEN [50] using branching fractions taken from the PDG [10], and the remaining unknown decays are modelled with LUNDCHARM [51]. Final state radiation (FSR) from charged final state particles is incorporated using PHOTOS [52].

3 Study of $e^+e^- \rightarrow \phi\chi_{c1,c2}$ with $\chi_{c1,c2} \rightarrow \gamma J/\psi$

3.1 Event Selection

For candidate events of interest, the ϕ meson is reconstructed from $K^+K^-/K_S^0K_L^0$, where the K_S^0 is reconstructed from $\pi^+\pi^-$ and the K_L^0 is missing due to the low detection efficiency with the BESIII detector. The $\chi_{c1,c2}$ is reconstructed from $\gamma J/\psi$, and the J/ψ is reconstructed from the lepton pairs e^+e^- or $\mu^+\mu^-$. The following event selection criteria are applied to both data and MC samples.

Charged tracks detected in the MDC are required to be within a polar angle (θ) range of $|\cos\theta| < 0.93$ (the coverage of the MDC), where θ is defined with respect to the z -axis, which is the symmetry axis of the MDC. For charged tracks not used for K_S^0 reconstruction, the distance of closest approach to the interaction point (IP) must be less than 10 cm along the z -axis, $|V_z| < 10$ cm, and less than 1 cm in the transverse plane, $|V_{xy}| < 1$ cm, while those for K_S^0 reconstruction, only a loose requirement of $|V_z| < 20$ cm is applied.

Photon candidates are identified using showers in the EMC. The deposited energy of each shower must be greater than 25 MeV in the barrel region ($|\cos\theta| < 0.80$) and greater than 50 MeV in the end cap region ($0.86 < |\cos\theta| < 0.92$). To exclude the showers that originate from charged tracks, the angle between the position of each shower in the EMC and the closest extrapolated charged track must be greater than 10 degrees. To suppress the electronic noise and the showers unrelated to the event, the difference between the EMC time and the event start time is required to be within $[0, 700]$ ns.

For each event, the lepton pair ($\ell^+\ell^-$) from J/ψ decays and the kaons from ϕ decays can be effectively distinguished by their momenta in the lab-frame. The tracks with momentum larger than 1 GeV/ c are assigned as leptons, and the amount of deposited energy in the EMC is further used to separate the muons from electrons. For both muon candidates, the deposited energy in the EMC is required to be less than 0.4 GeV, while it is required to be greater than 1.0 GeV for electrons. For the tracks with momentum less than 1 GeV/ c , particle identification (PID), which combines measurements of the energy deposited in the MDC (dE/dx) and the flight time in the TOF to form likelihoods $\mathcal{L}(h)$ ($h = K, \pi$) for each hadron h hypothesis, is used. Tracks are identified as kaons when the kaon hypothesis has a larger likelihood than the pion hypothesis ($\mathcal{L}(K) > \mathcal{L}(\pi)$ and $\mathcal{L}(K) > 0$).

3.1.1 3-track events with $\phi \rightarrow K^+K^-$

For the $\phi \rightarrow K^+K^-$ channel, one of the kaons could be missing due to an inefficiency. Together with the lepton pair from the J/ψ decay, there are three charged particles remaining in each signal event (referred to as the 3-track events). Two of the charged tracks are assigned as the lepton pair and the third as a kaon. The PID likelihood of the kaon is required to satisfy $\mathcal{L}(K) > \mathcal{L}(\pi)$ and $\mathcal{L}(K) > 0$, and at least one photon candidate is also required.

To improve the resolution and suppress background, a one-constraint (1C) kinematic fit is applied to the 3-track event by constraining the mass of the missing particle to the kaon nominal mass ($M(K_{\text{miss}}^\mp) = \sqrt{(P_{e^+e^-} - P_{\gamma K^\pm \ell^+ \ell^-})^2}$) inferred from the four momentum conservation. For the events with multiple photons in the final state, the combination of

$\gamma K^\pm K_{\text{miss}}^\mp \ell^+ \ell^-$ with the smallest χ^2 from the kinematic fit is retained, and $\chi^2 < 20$ is required.

To reduce the π misidentification background in the $\mu^+ \mu^-$ channel, the MUC is used to identify muons. At least one of muon candidate should have a hit depth > 30 cm in the MUC. To veto the radiative Bhabha background in $J/\psi \rightarrow e^+ e^-$ events, the polar angle of e^+ is required to satisfy $\cos(\theta_{e^+}) < 0.85$.

After imposing these selection criteria, there is a clear $\phi J/\psi$ event cluster in the 2-dimensional distribution of the $M(K^+ K^-)$ versus $M(\ell^+ \ell^-)$ as shown in Figure 1. The ϕ and J/ψ mass windows are defined as $0.995 \text{ GeV}/c^2 < M(K^+ K^-) < 1.050 \text{ GeV}/c^2$ (the mass resolution is $10 \text{ MeV}/c^2$) and $3.045 \text{ GeV}/c^2 < M(\ell^+ \ell^-) < 3.155 \text{ GeV}/c^2$ (the mass resolution is $17 \text{ MeV}/c^2$), respectively. To estimate the non- ϕ and non- J/ψ backgrounds, the ϕ sideband region is defined as $1.068 \text{ GeV}/c^2 < M(K^+ K^-) < 1.178 \text{ GeV}/c^2$, which is twice as wide as the ϕ signal region, while $2.90 \text{ GeV}/c^2 < M(\ell^+ \ell^-) < 3.01 \text{ GeV}/c^2$ and $3.19 \text{ GeV}/c^2 < M(\ell^+ \ell^-) < 3.30 \text{ GeV}/c^2$ are defined as the J/ψ sideband region, which is twice as wide as the J/ψ signal region (see Figure 1). Figure 1 also shows the invariant mass distributions of the $M(K^+ K^-)$, $M(\ell^+ \ell^-)$ and the 2-dimensional distribution of the $M(K^+ K^-)$ versus $M(\gamma J/\psi)$, where the events are clustered in the ϕ and $\chi_{c1,c2}$ mass regions.

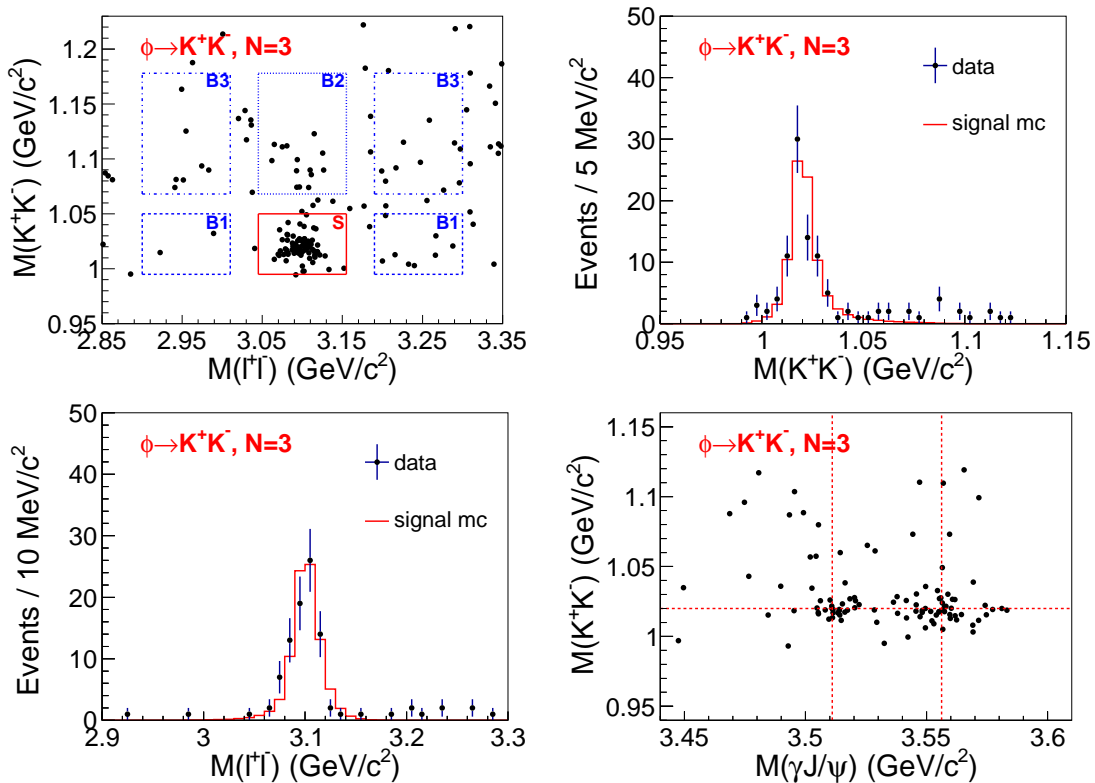


Figure 1. The 2-dimensional distribution of the $M(K^+K^-)$ versus $M(\ell^+\ell^-)$ (upper left), the invariant mass distributions of the $M(K^+K^-)$ (upper right), $M(\ell^+\ell^-)$ (bottom left) and the 2-dimensional distribution of the $M(K^+K^-)$ versus $M(\gamma J/\psi)$ (bottom right) for the 3-track events in the $\phi \rightarrow K^+K^-$ mode. Dots with and without error bars are the full data, the red histograms are the signal MC. In the upper left panel, the red solid box is the $\phi J/\psi$ signal region (S), the blue dashed, dotted and dash-dotted boxes indicate the ϕ non- J/ψ (B1), J/ψ non- ϕ (B2) and non- ϕ non- J/ψ (B3) sideband regions, respectively. The vertical (horizontal) dashed lines in the bottom right panel are central masses of χ_{c1}/χ_{c2} (ϕ).

3.1.2 4-track events with $\phi \rightarrow K^+K^-$

For a candidate event with $K^+K^-\ell^+\ell^-$ detected (referred to as 4-track events), the photon candidate is always ignored and not required to be detected in order to improve the efficiency. At least four charged tracks are required, two of which are assigned as the lepton pair and the remaining tracks as kaons. Both kaons are required to be identified. A similar 1C kinematic fit is performed by constraining the mass of the missing particle to be a photon inferred from the four momentum conservation, i.e. $M(\gamma_{\text{miss}}) = \sqrt{(P_{e^+e^-} - P_{K^+K^-\ell^+\ell^-})^2}$. The kinematic fit χ^2 is required to be $\chi^2 < 35$. The same MUC requirement as for 3-track events is applied to the muon candidates to suppress pion background.

Figure 2 shows the 2-dimensional distribution of the $M(K^+K^-)$ versus $M(\ell^+\ell^-)$, the invariant mass distributions of the $M(K^+K^-)$, $M(\ell^+\ell^-)$, and the 2-dimensional distribution of the $M(K^+K^-)$ versus $M(\gamma J/\psi)$ after the above selections. Clear ϕ and J/ψ resonance peaks are shown in the $M(K^+K^-)$ and $M(\ell^+\ell^-)$ distributions, and the events

are clearly clustered in the χ_{c1} and χ_{c2} mass regions in the $M(\gamma J/\psi)$ distribution, where the same mass window requirements defined in section 3.1.1 have been applied.

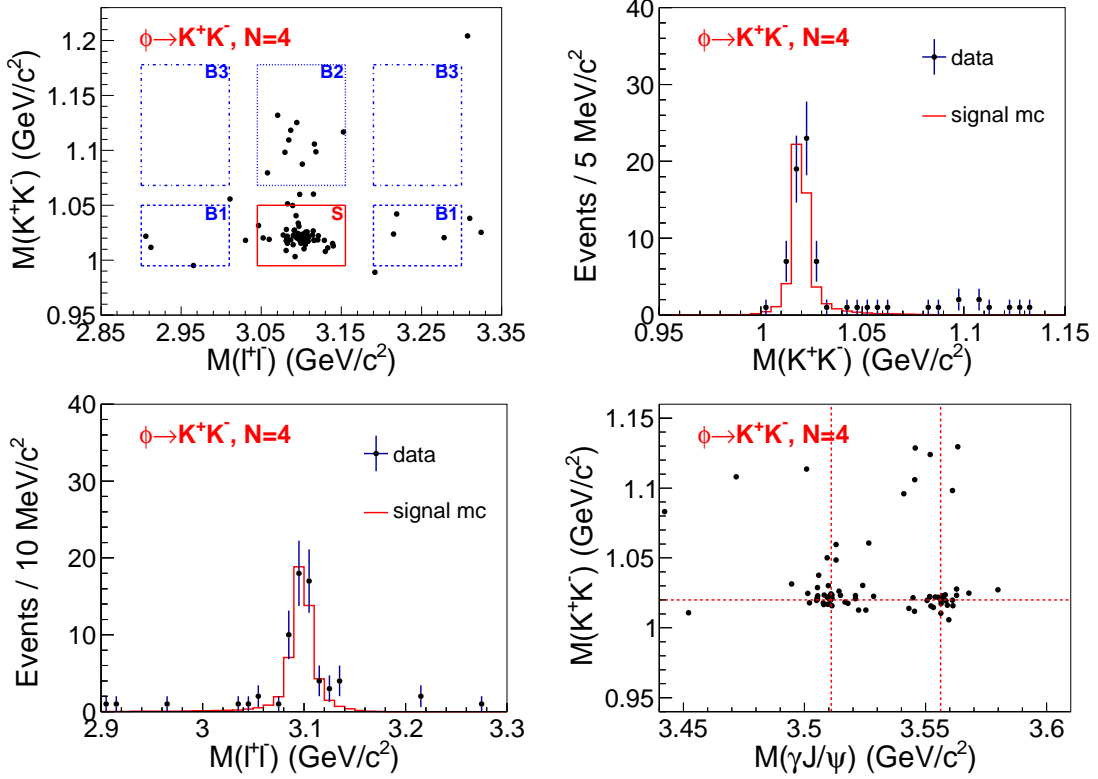


Figure 2. The 2-dimensional distribution of the $M(K^+K^-)$ versus $M(\ell^+\ell^-)$ (upper left), the invariant mass distributions of the $M(K^+K^-)$ (upper right), $M(\ell^+\ell^-)$ (bottom left) and the 2-dimensional distribution of the $M(K^+K^-)$ versus $M(\gamma J/\psi)$ (bottom right) for the 4-track events in the $\phi \rightarrow K^+K^-$ mode. Dots with and without error bars are the full data, the red histograms are the signal MC. In the upper left panel, the red solid box is the $\phi J/\psi$ signal region (S), the blue dashed, dotted and dash-dotted boxes indicate the ϕ non- J/ψ (B1), J/ψ non- ϕ (B2) and non- ϕ non- J/ψ (B3) sideband regions, respectively. The vertical (horizontal) dashed lines in the bottom right panel are central masses of χ_{c1}/χ_{c2} (ϕ).

3.1.3 Events with $\phi \rightarrow K_S^0 K_L^0$

The events from $\phi \rightarrow K_S^0 K_L^0$ decay are reconstructed with $K_S^0 \rightarrow \pi^+\pi^-$. The neutral K_L^0 candidate has a long lifetime and is not detected. We require at least four charged tracks to be detected in each event, two of which are assigned as the lepton pair and the remaining charged tracks are pions. The K_S^0 candidates are reconstructed from two oppositely charged pions satisfying $|V_z| < 20$ cm. There is no PID requirement for the charged pions, and they are constrained to originate from a common secondary decay vertex. The decay length of the K_S^0 candidate is required to be greater than twice the vertex resolution away from the IP to suppress the non- K_S^0 background. After the vertex fit, we set a mass window of $0.490 \text{ GeV}/c^2 < M(\pi^+\pi^-) < 0.505 \text{ GeV}/c^2$ for the K_S^0 candidate (the mass resolution is $5 \text{ MeV}/c^2$). At least one good photon candidate is also required in each event.

A 1C kinematic fit is applied to each event, with the mass of the missing particle constrained to the K_L^0 nominal mass inferred from the four momentum conservation, i.e. $M(K_{L\text{miss}}^0) = \sqrt{(P_{e^+e^-} - P_{\gamma K_S^0 \ell^+ \ell^-})^2}$. The kinematic fit χ^2 is required to be $\chi^2 < 20$.

After applying these requirements, clear ϕ and J/ψ resonance peaks are observed in the $RM(\gamma J/\psi)$ and $M(\ell^+ \ell^-)$ mass distributions as shown in Figure 3, where $RM(\gamma J/\psi) = \sqrt{(P_{e^+e^-} - P_{\gamma J/\psi})^2}$ is the recoil mass from the $\gamma J/\psi$ system. We define the ϕ and J/ψ mass windows as $0.998 \text{ GeV}/c^2 < RM(\gamma J/\psi) < 1.048 \text{ GeV}/c^2$ (the mass resolution is $9 \text{ MeV}/c^2$) and $3.050 \text{ GeV}/c^2 < M(\ell^+ \ell^-) < 3.154 \text{ GeV}/c^2$ (the mass resolution is $16 \text{ MeV}/c^2$), respectively, as shown in Figure 3. The ϕ sideband is defined as $1.065 \text{ GeV}/c^2 < RM(\gamma J/\psi) < 1.165 \text{ GeV}/c^2$, which is twice as wide as the ϕ signal region, and the J/ψ sidebands are defined as $2.911 \text{ GeV}/c^2 < M(\ell^+ \ell^-) < 3.015 \text{ GeV}/c^2$ and $3.189 \text{ GeV}/c^2 < M(\ell^+ \ell^-) < 3.293 \text{ GeV}/c^2$, which is twice as wide as the J/ψ signal region. Figure 3 also shows the 2-dimensional distribution of the $RM(\gamma J/\psi)$ versus $M(\gamma J/\psi)$, where the events are clearly clustered in the χ_{c1} and χ_{c2} mass regions in the $M(\gamma J/\psi)$ distribution.

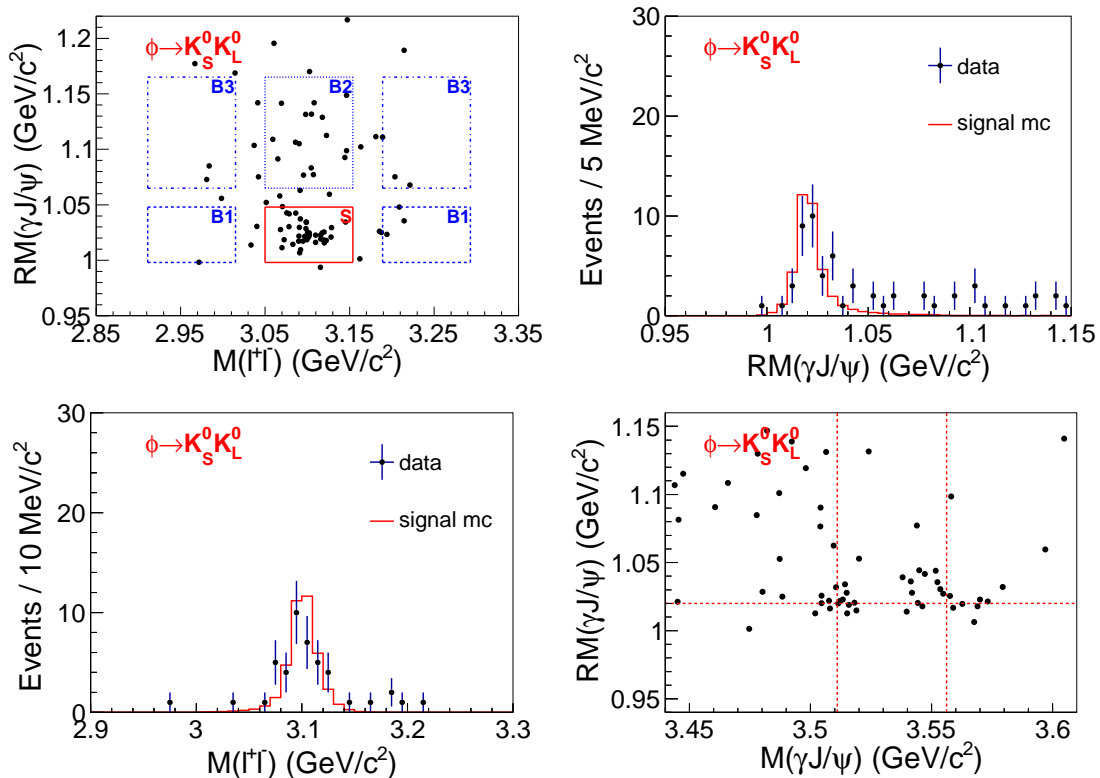


Figure 3. The 2-dimensional distribution of the $RM(\gamma J/\psi)$ versus $M(\ell^+\ell^-)$ (upper left), the invariant mass distributions of the $RM(\gamma J/\psi)$ (upper right), $M(\ell^+\ell^-)$ (bottom left) and the 2-dimensional distribution of the $RM(\gamma J/\psi)$ versus $M(\gamma J/\psi)$ (bottom right) in the $\phi \rightarrow K_S^0 K_L^0$ mode. Dots with and without error bars are the full data, the red histograms are the signal MC. In the upper left panel, the red solid box is the $\phi J/\psi$ signal region (S), the blue dashed, dotted and dash-dotted boxes indicate the ϕ non- J/ψ (B1), J/ψ non- ϕ (B2) and non- ϕ non- J/ψ (B3) sideband regions, respectively. The vertical (horizontal) dashed lines in the bottom right panel are central masses of χ_{c1}/χ_{c2} (ϕ).

3.2 Cross section measurement

Based on the event selection, the χ_{c1} and χ_{c2} signals are observed from both the $\phi \rightarrow K^+ K^-$ and $K_S^0 K_L^0$ modes. To determine the signal yields, an unbinned maximum likelihood fit is performed to the $M(\gamma J/\psi)$ distribution in the $\phi \rightarrow K^+ K^-$ and $K_S^0 K_L^0$ modes simultaneously. In the fit at each c.m. energy, the signal probability-density-function (PDF) is described by a MC-simulated shape convolved with a Gaussian function, which models the resolution difference between data and MC simulation. The MC-simulated shape is a weighted sum of the simulations at each c.m. energy, which has already taken into account the c.m. energy and decay modes dependence for the resolution. The Gaussian parameters are determined from the fit to the full dataset which has higher statistics. A linear function is used to describe the background. The two modes share the same $\phi\chi_{c1,c2}$ production cross section at the same c.m. energy. The selection efficiencies and branching fractions of the $\phi \rightarrow K^+ K^- / K_S^0 K_L^0$ modes at each c.m. energy are included in the fit.

Figure 4 shows the fit result for the full dataset from $\sqrt{s} = 4.600$ GeV to 4.951 GeV, and the corresponding plots at each individual c.m. energy are shown in Figure 9 of Appendix A. The statistical significance is estimated by comparing the fit likelihoods with and without the $\chi_{c1,c2}$ signal. In addition to the nominal fit, the fits by changing the background shape and the fit range have also been performed. In all the cases, the significance of the $\chi_{c1,c2}$ is found to be greater than 10σ , by comparing the difference of log-likelihoods $\Delta(-2\ln\mathcal{L}) = 137(131)$ for the $\chi_{c1}(\chi_{c2})$ and taking into account the change of the number of degrees of freedom ($\Delta\text{d.o.f.} = 5$).

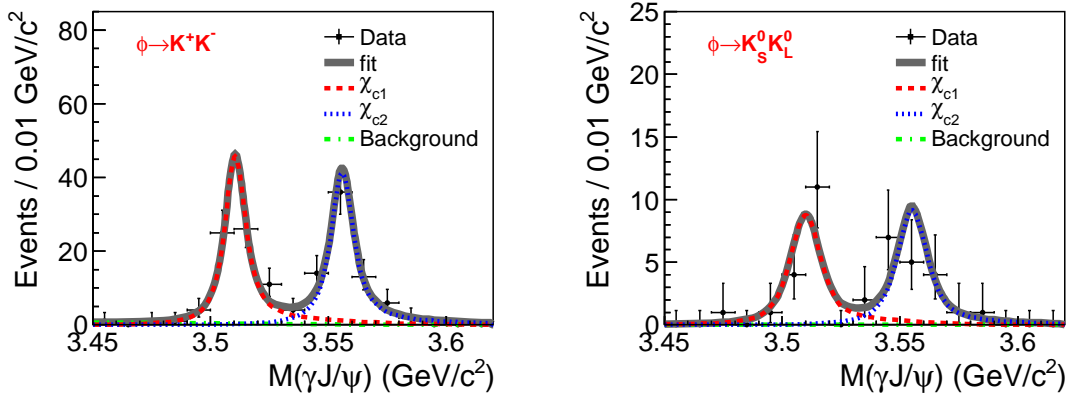


Figure 4. Sum of the simultaneous fits to $M(\gamma J/\psi)$ distribution for the full data sets. Dots with error bars are the data, the solid curves are the fit results, the red dashed, blue dotted, and green dash-dotted lines are the χ_{c1} , χ_{c2} and the background shape, respectively.

The Born cross section of $e^+e^- \rightarrow \phi\chi_{c1,c2}$ at c.m. energy \sqrt{s} is calculated with

$$\sigma^B(\sqrt{s}) = \frac{N^{\text{fit}}}{\mathcal{L}_{\text{int}}(1+\delta)\frac{1}{|1-\Pi|^2}\mathcal{B}}, \quad (3.1)$$

where N^{fit} is the number of fitted events for the $\phi\chi_{c1,c2}$, which is equal to the number of the $\phi\chi_{c1,c2}$ events in data divided by the efficiency and branching fraction of ϕ , \mathcal{L}_{int} is the integrated luminosity, $(1+\delta)$ is the ISR correction factor obtained from KKMC, $\frac{1}{|1-\Pi|^2}$ is the vacuum polarization factor [53], and \mathcal{B} is the product of the branching fraction for $\chi_{c1,c2} \rightarrow \gamma J/\psi$ and $J/\psi \rightarrow \ell^+\ell^-$. The Born cross sections of $e^+e^- \rightarrow \phi\chi_{c1}$ and $e^+e^- \rightarrow \phi\chi_{c2}$ at each c.m. energy are listed in Tables 1 and 2, respectively. In case the signal significance is less than 3σ , an upper limit of the Born cross section ($\sigma^{\text{U.L.}}$) at the 90% confidence level (C.L.) is also reported. The upper limits of $\phi\chi_{c1}$ and $\phi\chi_{c2}$ yields are estimated via a Bayesian approach [10]. A likelihood scan $L(n)$ is performed with various assumptions for the number of signal events (n) in the fit. The systematic uncertainty is also considered by smearing the likelihood distribution with a Gaussian function with width equal to the systematic uncertainty. The upper limit of $N^{\text{U.L.}}$ at the 90% C.L. corresponds to $\int_0^{N^{\text{U.L.}}} L(x)dx / \int_0^\infty L(x)dx = 0.9$. The detection efficiencies of $\phi\chi_{c1,c2}$ events depend on the e^+e^- c.m. energy. With the increasing c.m. energy, charged kaons have higher momentum and are thus much more efficient to be detected, while for the $K_S^0K_L^0$ channel,

due to more ISR events the reconstruction efficiency whereas decreases (the $\pi^+\pi^-$ from K_S^0 decay already have sufficient momentum to be detected and are not sensitive to c.m. energy).

\sqrt{s} (GeV)	\mathcal{L}_{int} (pb $^{-1}$)	$\epsilon_{K^+K^-}^3$	$\epsilon_{K^+K^-}^4$	$\epsilon_{K_S^0K_L^0}$	$\frac{1+\delta}{ 1-\Pi ^2}$	N^{fit}	σ^{B} (pb)
4.600	586.9	0.261	0.092	0.229	0.88	$56.0_{-15.1}^{+18.2}$	$2.63_{-0.71}^{+0.86} \pm 0.20$ (5.8σ)
4.612	103.8	0.257	0.101	0.223	0.90	$13.3_{-6.3}^{+9.4}$ (< 29.8)	$3.45_{-1.64}^{+2.43} \pm 0.25$ (< 7.7)
4.628	521.5	0.247	0.120	0.224	0.92	$54.7_{-14.3}^{+17.3}$	$2.77_{-0.73}^{+0.88} \pm 0.20$ (3.3σ)
4.641	552.4	0.245	0.133	0.222	0.94	$60.4_{-15.4}^{+18.6}$	$2.83_{-0.72}^{+0.87} \pm 0.20$ (5.3σ)
4.661	529.6	0.233	0.156	0.220	0.97	$21.5_{-8.4}^{+11.3}$	$1.02_{-0.39}^{+0.53} \pm 0.07$ (3.6σ)
4.682	1669.3	0.219	0.176	0.218	0.99	$79.4_{-18.5}^{+21.5}$	$1.17_{-0.27}^{+0.32} \pm 0.08$ (5.6σ)
4.699	536.5	0.208	0.188	0.213	1.02	$34.7_{-11.3}^{+14.3}$	$1.54_{-0.50}^{+0.63} \pm 0.11$ (4.4σ)
4.740	164.3	0.188	0.215	0.210	1.07	$20.2_{-9.8}^{+10.4}$ (< 37.5)	$2.80_{-1.35}^{+1.44} \pm 0.19$ (< 5.2)
4.750	367.2	0.181	0.214	0.208	1.09	$22.2_{-9.3}^{+12.2}$ (< 42.0)	$1.35_{-0.57}^{+0.74} \pm 0.10$ (< 2.5)
4.781	512.8	0.163	0.222	0.201	1.13	$0.0_{-0.0}^{+1.3}$ (< 13.5)	$0.0_{-0.0}^{+0.23} \pm 0.02$ (< 0.6)
4.843	527.3	0.142	0.228	0.188	1.24	$4.5_{-3.1}^{+6.0}$ (< 17.2)	$0.17_{-0.12}^{+0.22} \pm 0.01$ (< 0.6)
4.918	208.1	0.115	0.214	0.167	1.41	$15.3_{-7.3}^{+10.7}$ (< 34.3)	$1.27_{-0.61}^{+0.89} \pm 0.09$ (< 2.8)
4.951	160.4	0.106	0.208	0.155	1.50	$5.3_{-3.7}^{+7.1}$ (< 20.4)	$0.53_{-0.37}^{+0.72} \pm 0.04$ (< 2.1)

Table 1. The Born cross section σ^{B} for $e^+e^- \rightarrow \phi\chi_{c1}$ at each c.m. energy (\sqrt{s}). The numbers in the brackets are the signal significances or upper limits $\sigma^{\text{U.L.}}$ at the 90% C.L. in case the signal significance is less than 3σ . The table also includes integrated luminosity \mathcal{L}_{int} , detection efficiency $\epsilon_{K^+K^-}^3$, $\epsilon_{K^+K^-}^4$ and $\epsilon_{K_S^0K_L^0}$ for the 3-track events of the $\phi \rightarrow K^+K^-$ mode, 4-track events of the $\phi \rightarrow K^+K^-$ mode and the events of the $\phi \rightarrow K_S^0K_L^0$ mode, respectively, the product of radiative correction factor and vacuum polarization factor $\frac{1+\delta}{|1-\Pi|^2}$ and the number of fitted events N^{fit} (also the corresponding upper limit $N^{\text{U.L.}}$ at the 90% C.L. in case the signal significance is less than 3σ). The first uncertainty is statistical and the second is systematic.

\sqrt{s} (GeV)	$\mathcal{L}_{\text{int}}(\text{pb}^{-1})$	$\epsilon_{K^+K^-}^3$	$\epsilon_{K^+K^-}^4$	$\epsilon_{K_S^0 K_L^0}$	$\frac{1+\delta}{ 1-\Pi ^2}$	N^{fit}	σ^{B} (pb)
4.600	586.9	0.253	0.031	0.226	0.73	$26.7_{-11.0}^{+14.6}$	$2.73_{-1.13}^{+1.49} \pm 0.27$ (3.6σ)
4.612	103.8	0.257	0.047	0.215	0.75	$9.8_{-5.6}^{+8.9}$ (< 26.6)	$5.50_{-3.14}^{+5.02} \pm 0.61$ (< 15.0)
4.628	521.5	0.261	0.070	0.222	0.76	$15.1_{-7.8}^{+11.0}$ (< 34.0)	$1.67_{-0.86}^{+1.22} \pm 0.17$ (< 3.8)
4.641	552.4	0.263	0.086	0.225	0.77	$24.4_{-10.9}^{+13.9}$	$2.52_{-1.12}^{+1.44} \pm 0.27$ (3.6σ)
4.661	529.6	0.259	0.112	0.230	0.80	$45.5_{-12.7}^{+15.6}$	$4.71_{-1.32}^{+1.61} \pm 0.42$ (6.4σ)
4.682	1669.3	0.255	0.137	0.234	0.84	$136.3_{-24.2}^{+26.9}$	$4.26_{-0.76}^{+0.84} \pm 0.42$ (9.5σ)
4.699	536.5	0.245	0.152	0.232	0.88	$81.9_{-17.3}^{+20.0}$	$7.61_{-1.61}^{+1.86} \pm 1.02$ (8.2σ)
4.740	164.3	0.219	0.181	0.226	1.01	$0.0_{-0.0}^{+1.3}$ (< 9.9)	$0.0_{-0.0}^{+1.36} \pm 0.26$ (< 2.6)
4.750	367.2	0.208	0.184	0.221	1.04	$6.5_{-5.3}^{+8.9}$ (< 23.5)	$0.75_{-0.61}^{+1.02} \pm 0.13$ (< 2.7)
4.781	512.8	0.179	0.194	0.209	1.12	$17.2_{-7.2}^{+10.1}$ (< 34.5)	$1.31_{-0.55}^{+0.77} \pm 0.13$ (< 2.6)
4.843	527.3	0.145	0.196	0.180	1.28	$0.0_{-0.0}^{+1.3}$ (< 11.2)	$0.0_{-0.0}^{+0.40} \pm 0.03$ (< 0.7)
4.918	208.1	0.113	0.189	0.160	1.44	$5.0_{-3.9}^{+7.6}$ (< 21.1)	$0.73_{-0.57}^{+1.11} \pm 0.06$ (< 3.1)
4.951	160.4	0.107	0.183	0.151	1.51	$0.0_{-0.0}^{+1.3}$ (< 13.0)	$0.0_{-0.0}^{+1.31} \pm 0.11$ (< 2.4)

Table 2. The Born cross section σ^{B} for $e^+e^- \rightarrow \phi\chi_{c2}$ at each c.m. energy (\sqrt{s}). The numbers in the brackets are the signal significances or upper limits $\sigma^{\text{U.L.}}$ at the 90% C.L. in case the signal significance is less than 3σ . The table also includes integrated luminosity \mathcal{L}_{int} , detection efficiency $\epsilon_{K^+K^-}^3$, $\epsilon_{K^+K^-}^4$ and $\epsilon_{K_S^0 K_L^0}$ for the 3-track events of the $\phi \rightarrow K^+K^-$ mode, 4-track events of the $\phi \rightarrow K^+K^-$ mode and the events of the $\phi \rightarrow K_S^0 K_L^0$ mode, respectively, the product of radiative correction factor and vacuum polarization factor $\frac{1+\delta}{|1-\Pi|^2}$, and the number of fitted events N^{fit} (also the corresponding upper limit $N^{\text{U.L.}}$ at the 90% C.L. in case the signal significance is less than 3σ). The first uncertainty is statistical and the second is systematic.

To investigate the \sqrt{s} -dependent cross section line shape of $e^+e^- \rightarrow \phi\chi_{c1,c2}$, a maximum likelihood fit is performed to the dressed cross section ($\sigma^{\text{B}}(\sqrt{s})\frac{1}{|1-\Pi|^2}$). Due to the small numbers of events at each single c.m. energy, the likelihood function is constructed as

$$\mathcal{L} = \prod_i P(N_i^{\text{obs}}; N_i^{\text{exp}} + N_i^{\text{bkg}}) \quad (3.2)$$

where P represents a Poisson distribution, N_i^{obs} , N_i^{exp} and N_i^{bkg} are the number of observed events, the number of expected $\chi_{c1,c2}$ signal events and the background events in the $\chi_{c1,c2}$ signal region for the i -th dataset, respectively. Here in the fit, only statistical uncertainties are considered.

For the $e^+e^- \rightarrow \phi\chi_{c1}$ process, a continuum amplitude is used to fit the cross section,

$$A_{\text{cont}}(\sqrt{s}) = \sqrt{\frac{f_{\text{cont}}}{(\sqrt{s}/4.682)^n}}, \quad (3.3)$$

where f_{cont} and n are free parameters in the fit. We also use a phase space (PHSP) shape corrected continuum amplitude $A_{\text{cont}}(\sqrt{s})\sqrt{\Phi(\sqrt{s})}$ to fit the cross section, where $\Phi(\sqrt{s})$ is the two-body PHSP factor. Figure 5 shows the fit results with both models, and the numerical results are listed in Table 3. We also fit the cross section data with a Breit-Wigner (BW) function and the coherent sum of a BW and a continuum amplitude, and no significant resonance structures are found.

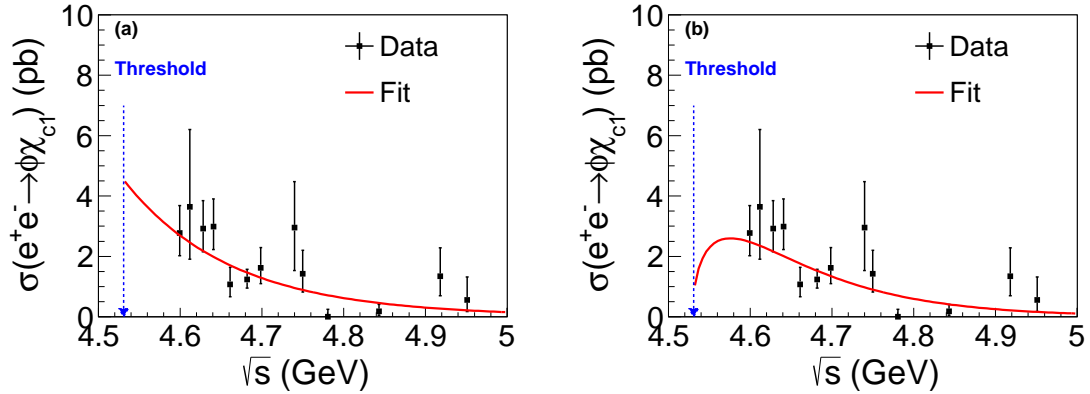


Figure 5. Fit to the cross section of $e^+e^- \rightarrow \phi\chi_{c1}$ with (a) the continuum amplitude and (b) the PHSP corrected continuum amplitude.

Parameter	$ A_{\text{cont}} ^2$	$ A_{\text{cont}}\sqrt{\Phi} ^2$
f_{cont}	1.47 ± 0.16	14.26 ± 1.59
n	34.52 ± 8.34	48.94 ± 8.74
$\chi^2/\text{d.o.f.}$	21.6/11	21.9/11

Table 3. The numerical results for the fit to the cross section of $e^+e^- \rightarrow \phi\chi_{c1}$ with the pure continuum amplitude (2nd column) and PHSP corrected continuum amplitude (3rd column). The errors are statistical.

For the $e^+e^- \rightarrow \phi\chi_{c2}$ process, there is a possible resonance structure around 4.7 GeV in the cross section line shape as shown in Fig. 6, which is fitted with a BW function:

$$\text{BW}(\sqrt{s}) = \frac{M}{\sqrt{s}} \cdot \frac{\sqrt{12\pi\Gamma_{\text{tot}}\Gamma_{e^+e^-}\mathcal{B}(Y \rightarrow \phi\chi_{c2})}}{s - M^2 + iM\Gamma_{\text{tot}}} \cdot \sqrt{\frac{\Phi(\sqrt{s})}{\Phi(M)}} \quad (3.4)$$

where M , Γ_{tot} and $\Gamma_{e^+e^-}$ are the mass, full width, and electric width of the potential resonance Y , respectively, and $\mathcal{B}(Y \rightarrow \phi\chi_{c2})$ is the branching fraction of $Y \rightarrow \phi\chi_{c2}$. Figure 6 (a) shows the fit results, which yields

$$M = (4672.7 \pm 10.8) \text{ MeV}/c^2, \quad \Gamma_{\text{tot}} = (93.2 \pm 19.8) \text{ MeV}, \quad (3.5)$$

for the resonance. A χ^2 test method is used to estimate the fit quality, which gives $\chi^2/\text{d.o.f.} = 15.9/10$. The significance for the resonance hypothesis over the continuum hypothesis is estimated to be 3.1σ , by comparing the difference of log-likelihoods $\Delta(-2\ln\mathcal{L}) = 10.0$ and taking into account the change of number of degree of freedom ($\Delta\text{d.o.f.} = 1$). Here the continuum hypothesis follows $A_{\text{cont}}(\sqrt{s})\sqrt{\Phi(\sqrt{s})}$. The fit result for the continuum hypothesis is shown in Figure 6 (a) (dash-dotted line) and listed in Table 4 (last column).

The potential resonance (solid line in Figure 6 (a)) is found to be consistent with the $Y(4660)$ reported in $e^+e^- \rightarrow \pi^+\pi^-\psi(3686)$ [5–8]. Next, we fit the $e^+e^- \rightarrow \phi\chi_{c2}$ cross section with the fixed mass and width of the $Y(4660)$ [8]. Two fit models are considered: one is the single BW model, which gives $\Gamma_{e^+e^-}\mathcal{B}[Y(4660) \rightarrow \phi\chi_{c2}] = 1.0 \pm 0.1$ eV with a fit quality $\chi^2/\text{d.o.f.} = 21.5/12$ (the dashed line in Figure 6 (a)), and the other is the coherent sum of a BW and PHSP model ($\text{BW} + f\sqrt{\Phi}e^{i\phi}$), which gives $\Gamma_{e^+e^-}\mathcal{B}[Y(4660) \rightarrow \phi\chi_{c2}] = 1.2 \pm 0.4$ eV with a fit quality $\chi^2/\text{d.o.f.} = 17.9/10$ (the dotted line in Figure 6 (a)). Since the fit quality with the fixed $Y(4660)$ is close to the one with a single free BW model ($\chi^2/\text{d.o.f.} = 15.9/10$), we cannot distinguish between these two models.

To improve the fit quality, the fit model is parameterized as the coherent sum of a BW resonance and a possible continuum term ($\text{BW} + A_{\text{cont}}e^{i\phi}$). The fit result is shown in Figure 6 (b), which gives

$$M = (4701.8 \pm 10.9) \text{ MeV}/c^2, \Gamma_{\text{tot}} = (30.5 \pm 22.3) \text{ MeV} \quad (3.6)$$

for the resonance. The fit quality is $\chi^2/\text{d.o.f.} = 7.3/7$, and the significance for the resonance hypothesis is estimated using the same method, which gives 3.6σ ($\Delta(-2\ln\mathcal{L}) = 20.7$, $\Delta\text{d.o.f.} = 4$). All the numerical results of the fits are summarized in Table 4.

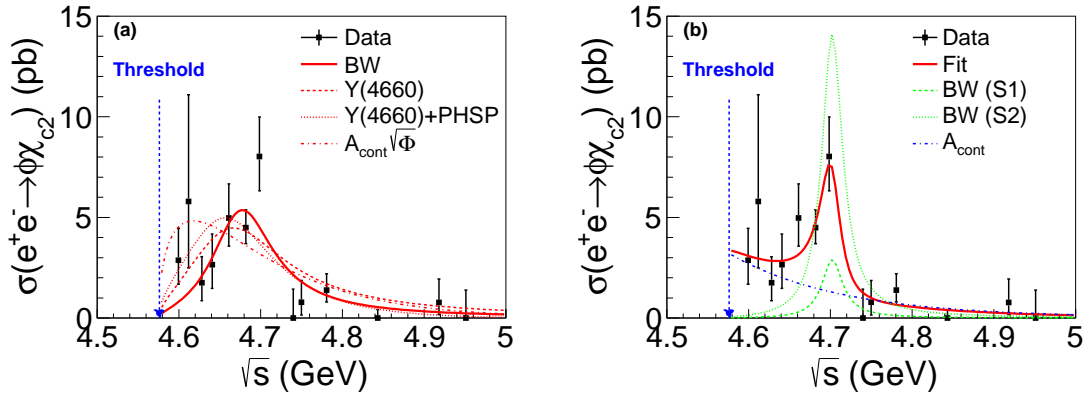


Figure 6. (a) Fit to the cross section of $e^+e^- \rightarrow \phi\chi_{c2}$ with a single BW (solid line), the $Y(4660)$ resonance hypothesis (dashed line), the coherent sum of $Y(4660)$ and PHSP (dotted line), and the PHSP corrected continuum amplitude as the non-resonance hypothesis (dash-dotted line). (b) Fit to the cross section of $e^+e^- \rightarrow \phi\chi_{c2}$ with the coherent sum of a BW and continuum amplitude. The solid line is the fit result, the dashed and dotted lines correspond to the BW with constructive (S1) and destructive (S2) solutions of interference, and the dash-dotted line is the continuum term.

The significance for the coherent sum of a BW and continuum model ($\text{BW} + A_{\text{cont}}e^{i\phi}$)

over the single BW model is estimated to be 2.3σ . Thus, we are not able to distinguish these two models based on the current data.

Parameter	$ \text{BW} ^2$	$ \text{BW} + A_{\text{cont}}e^{i\phi} ^2$ (S1)	$ \text{BW} + A_{\text{cont}}e^{i\phi} ^2$ (S2)	$ A_{\text{cont}}\sqrt{\Phi} ^2$
M (MeV/ c^2)	4672.75 ± 10.80		4701.77 ± 10.89	-
Γ_{tot} (MeV)	93.15 ± 19.78		30.50 ± 22.33	-
$\mathcal{B}\Gamma_{e^+e^-}$ (eV)	0.74 ± 0.13	0.13 ± 0.13	0.66 ± 0.41	-
f_{cont}	-		1.48 ± 0.72	40.61 ± 4.57
n	-		33.95 ± 22.24	54.28 ± 8.87
ϕ ($^\circ$)	-	240.20 ± 40.53	109.77 ± 13.57	-
$\chi^2/\text{d.o.f}$	15.9/10		7.3/7	26.9/11
Significance	3.1σ		3.6σ	-

Table 4. The numerical results for the fits to the cross section of $e^+e^- \rightarrow \phi\chi_{c2}$ with the single BW model (2nd column), the coherent sum of a BW and continuum model (3rd and 4th columns correspond to the constructive (S1) and destructive (S2) solutions of the interference), and PHSP corrected continuum model (5th column). The errors are statistical.

Since no obvious structures are observed in the $\phi\chi_{c1}$ mode, the upper limit of $\Gamma_{e^+e^-}\mathcal{B}(Y \rightarrow \phi\chi_{c1})$ is also determined for the possible structures observed in the $\phi\chi_{c2}$ mode. A similar method by scanning the $\Gamma_{e^+e^-}\mathcal{B}(Y \rightarrow \phi\chi_{c1})$ dependent likelihood distribution is used, and the results at 90% C.L. are listed in Table 5.

Resonance	$\Gamma_{e^+e^-}\mathcal{B}(Y \rightarrow \phi\chi_{c1})$ (eV)
BW ₁	< 0.07 at 90% C.L.
BW ₂	< 0.04 at 90% C.L.
$Y(4660)$ [8]	< 0.36 at 90% C.L.

Table 5. The upper limit of $\Gamma_{e^+e^-}\mathcal{B}(Y \rightarrow \phi\chi_{c1})$ at 90% C.L. for the possible structures in $\phi\chi_{c2}$, where BW₁ and BW₂ correspond to Equations (3.5) and (3.6), respectively.

3.3 Systematic uncertainty

3.3.1 Systematic uncertainty for cross section measurement

The sources of systematic uncertainties in the cross section measurement of $e^+e^- \rightarrow \phi\chi_{c1,c2}$ include the luminosity measurement, tracking efficiency, PID efficiency, K_S^0 reconstruction, photon reconstruction, kinematic fit, radiative correction, MC model, MUC response, branching ratios, and the fit.

The uncertainty of the integrated luminosity measurement is 0.6% by analyzing the large angle Bhabha events at BESIII [42]. The uncertainty of the tracking efficiency for high momentum leptons is 1% per track, and thus 2% by adding both leptons linearly [54] since we require both leptons detected. For the $\phi \rightarrow K^+K^-$ mode, both one kaon events and two kaon events are reconstructed. Assuming p (q) is the corresponding tracking efficiency for a single kaon from data (MC), the efficiency to reconstruct both one and two kaon candidates is $2p(1-p) + p^2 = 1 - (1-p)^2 [1 - (1-q)^2]$ for data (MC). Considering $p \approx 85\%$ and the tracking efficiency uncertainty $p/q - 1 = 1\%$ at BESIII, the uncertainty

due to the detection of both one and two kaon candidates for the tracking efficiency can be calculated as $\left|1 - \frac{1-(1-p)^2}{1-(1-q)^2}\right|$, which is negligible. The same calculation can be applied to the kaon PID uncertainty, which is also negligible. For the $\phi \rightarrow K_S^0 K_L^0$ mode, the uncertainty of tracking efficiency is 1% per pion. The uncertainty of K_S^0 reconstruction is estimated to be 1.2% by studying the $J/\psi \rightarrow K^*(892)^\pm K^\mp \rightarrow K_S^0 \pi^\pm K^\mp$ and $J/\psi \rightarrow \phi K_S^0 K^\mp \pi^\pm$ control samples [55]. The uncertainty from photon reconstruction is estimated to be 1% per photon by studying the $J/\psi \rightarrow \rho^0 \pi^0$ events [56].

The systematic uncertainty associated with kinematic fitting is estimated by comparing the efficiency difference with or without the helix parameters correction in MC simulations [57]. The radiative correction factor and efficiency depend on the input cross section line shape in KKMC. Using different cross section line-shapes as studied in section 3.2, the difference in $(1 + \delta)\epsilon$ between different models is taken as the systematic uncertainty. In the signal MC simulation, a phase space model is used. To estimate the uncertainty due to the MC model, the angular distribution of $e^+e^- \rightarrow \phi \chi_{c1,c2}$ is modelled by a $1 \pm \cos^2 \theta$ distribution, and the efficiency difference is taken as the systematic uncertainty.

The uncertainty from the MUC response is studied with a control sample of $e^+e^- \rightarrow \mu^+\mu^-$ events. The difference in efficiency between the data and MC simulation due to the requirement of μ hit depth in the MUC is taken as the systematic uncertainty. The uncertainties of branching fractions of the intermediate states are taken from the PDG [10]. The uncertainties related to the fit are investigated by changing the fit range and changing the background shape from a free 1st-order polynomial to a fixed flat shape with the number of events estimated from ϕ and J/ψ sidebands. The largest difference in signal yields is taken as the systematic uncertainty.

In section 3, three data samples, which are the 3-track events, 4-track events with $\phi \rightarrow K^+K^-$ and the events with $\phi \rightarrow K_S^0 K_L^0$, are reconstructed. A source of systematic uncertainty can contribute differently to the three data samples. To propagate the systematic uncertainty to the cross section, we take the weighted average of the systematic uncertainties in the three data samples, which follows

$$\sigma_{\text{tot}}^2 = \sum_{i=1}^3 \omega_i^2 \sigma_i^2 + 2 \sum_{i \neq j}^3 \text{cov}(i, j), \quad (3.7)$$

$$\omega_i = \frac{\epsilon_i \mathcal{B}_i}{\sum_{i=1}^3 \epsilon_i \mathcal{B}_i}, \quad \text{cov}(i, j) = \rho_{ij} \omega_i \omega_j \sigma_i \sigma_j, \quad (3.8)$$

where σ_{tot} is the average systematic uncertainty to the cross section as listed in Table 6, ω_i and σ_i are the weight and systematic uncertainty for i th data sample, ϵ_i and \mathcal{B}_i are the efficiency and branching ratio of ϕ for the i th data sample, ρ_{ij} is the correlation parameter between the i th and j th data samples, and $\rho_{ij} = 1$ if the systematic uncertainty is correlated between the i th and j th data samples, otherwise $\rho_{ij} = 0$.

Assuming all these sources are independent, the total systematic uncertainty in the cross section measurement is obtained by adding them in quadrature. Table 6 summarizes all the systematic sources and their contributions at 4.68 GeV, and the systematic uncertainties at other energy points are listed in Tables 13 and 14 of Appendix B.

Source	$\phi\chi_{c1}$	$\phi\chi_{c2}$
Luminosity	0.60	0.60
Tracking	2.42	2.44
Photon	0.65	0.73
K_S^0 reconstruction	0.25	0.27
Kinematic fit	0.49	0.52
$\mathcal{B}(\phi)$	0.83	0.82
$\mathcal{B}(\chi_{cJ})$	2.90	2.60
$\mathcal{B}(J/\psi)$	0.60	0.60
Radiative correction	0.40	5.31
MC model	0.18	0.16
Muon hit depth	0.86	0.85
Fit related	5.54	7.14
Total	6.93	9.74

Table 6. The systematic uncertainty sources and their contributions (in %) for the cross section of $e^+e^- \rightarrow \phi\chi_{c1,c2}$ at 4.68 GeV.

3.3.2 Systematic uncertainties for the resonance parameters

The systematic uncertainties for the resonance parameters mainly come from the absolute c.m. energy calibration, the parameterization of the BW function, and the cross section measurement.

The c.m. energies of the data sets used in this work are measured with Λ_c events, with an uncertainty of ± 0.6 MeV [42, 43]. This common uncertainty for all the data samples could shift the cross section line-shape globally, and is thus the systematic uncertainty to the mass of the resonance.

In the fit to the cross section of $e^+e^- \rightarrow \phi\chi_{c2}$ (Figure 6), a constant full width BW function is employed. We also use an alternative BW function, where the constant width is replaced by an energy dependent width $\Gamma(\sqrt{s}) = \Gamma_0 \cdot \frac{\sqrt{s}}{M}$. Here Γ_0 is the full width at $\sqrt{s} = M$. The difference in the resonance parameters between the two BWs is taken as the systematic uncertainty.

In the fit to the cross section of $e^+e^- \rightarrow \phi\chi_{c2}$ (Figure 6 (b)), a continuum amplitude (Equation (3.3)) is used to describe the non-resonance contribution. We also use a PHSP corrected continuum amplitude ($A_{\text{cont}}\sqrt{\Phi}$) in the fit. The difference in the resonance parameters is taken as the systematic uncertainty.

The uncertainty from the cross section measurement can be divided into two parts, one is the correlated systematic uncertainty for all the energy points, including tracking, photon reconstruction, K_S^0 reconstruction, luminosity, branching fraction, muon hit depth, background shape, and fit range. They are propagated to $\Gamma_{e^+e^-}\mathcal{B}(Y \rightarrow \phi\chi_{c2})$ directly. The other is the uncorrelated systematic uncertainty, which is dominated by the radiation correction according to the previous section. This uncertainty can be considered in the fit to the cross section. The two types of uncertainties are added in quadrature assuming they are independent.

Tables 7 and 8 summarize the sources of systematic uncertainty for the resonance parameters and their contributions, and the total systematic uncertainty is obtained by adding them in quadrature.

Source	Mass (MeV/ c^2)	Width (MeV)	$\mathcal{B}\Gamma_{e^+e^-}$ (eV)
c.m. energy	0.6	-	-
Parameterization of BW	0.04	0.70	0.01
Cross section	3.81	9.39	0.07
Total	3.86	9.42	0.07

Table 7. The systematic uncertainties for the resonance parameters with the single BW model.

Source	Mass (MeV/ c^2)	Width (MeV)	$\mathcal{B}\Gamma_{e^+e^-}$ [S1] (eV)	$\mathcal{B}\Gamma_{e^+e^-}$ [S2] (eV)
c.m. energy	0.6	-	-	-
Parameterization of BW	0.05	0.06	0.0	0.01
Parameterization of A_{cont}	2.12	13.51	0.05	0.27
Cross section	1.63	5.52	0.01	0.09
Total	2.74	14.59	0.05	0.29

Table 8. The systematic uncertainties for resonance parameters with the coherent sum of a BW and continuum.

4 Study of $e^+e^- \rightarrow \gamma X$ with $X \rightarrow \phi J/\psi$

The process of $e^+e^- \rightarrow \gamma X \rightarrow \gamma \phi J/\psi$ shares the same final states as that of $e^+e^- \rightarrow \phi \chi_{c1,c2}$, thus the same event selection criteria are applied to the $e^+e^- \rightarrow \gamma X$ process. The $M(\phi J/\psi)$ invariant mass distribution, shown in Figure 7, is well described by the $\phi \chi_{c1,c2}$ events, together with the non- $\gamma \phi J/\psi$ background events estimated from the ϕ - J/ψ 2-dimensional sidebands (B1/2 + B2/2 - B3/4 as exhibited in Figures 1 to 3). No other structure is observed in the $M(\phi J/\psi)$ mass distribution.

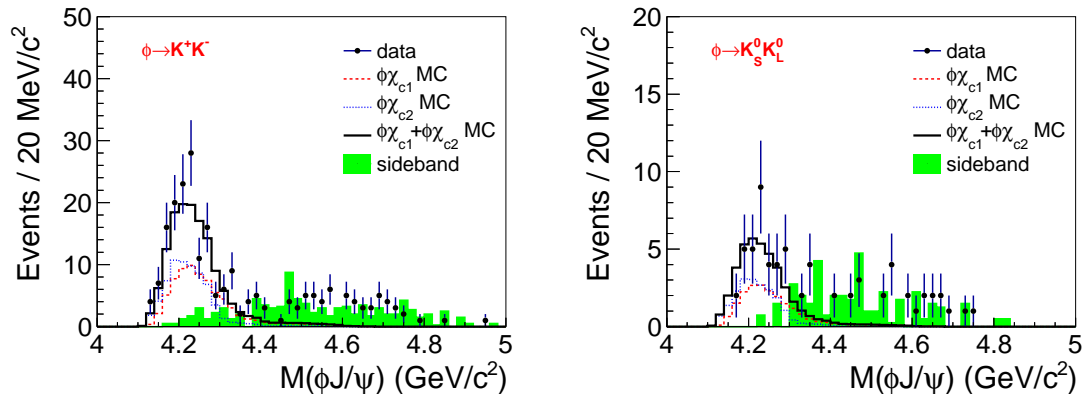


Figure 7. The invariant mass distribution of $M(\phi J/\psi)$ in the $\phi \rightarrow K^+K^-$ and $\phi \rightarrow K_S^0 K_L^0$ modes. Dots with error bars are the full data, the red dashed and blue dotted histograms are from $\phi\chi_{c1}$ and $\phi\chi_{c2}$ MC, which have been normalized to the data, the black solid histograms are the sum of $\phi\chi_{c1}$ and $\phi\chi_{c2}$, and the green filled histograms are the $\phi - J/\psi$ 2-dimensional sideband.

4.1 Upper limit of $e^+e^- \rightarrow \gamma X$ cross section

The product of Born cross section of $e^+e^- \rightarrow \gamma X$ and the branching fraction of $X \rightarrow \phi J/\psi$ is calculated by

$$\sigma_{\gamma X}^B \mathcal{B}(X \rightarrow \phi J/\psi) = \frac{N_{\gamma X}^{\text{fit}}}{\mathcal{L}_{\text{int}}(1 + \delta) \frac{1}{|1 - \Pi|^2} \mathcal{B}}, \quad (4.1)$$

where $N_{\gamma X}^{\text{fit}}$ is the number of fitted events for γX , which is equal to the number of γX events in data divided by the efficiency and branching fraction of ϕ , \mathcal{L}_{int} is the integrated luminosity, $1 + \delta$ is the ISR correction factor, $\frac{1}{|1 - \Pi|^2}$ is the vacuum polarization factor, and \mathcal{B} is the branching fraction of $J/\psi \rightarrow \ell^+\ell^-$.

Since no significant structures are observed, we determine the upper limit of the production cross section for $e^+e^- \rightarrow \gamma X \rightarrow \gamma\phi J/\psi$ using the same method as described in section 3.2. An unbinned maximum likelihood fit is performed to the $M(\phi J/\psi)$ distribution simultaneously for the $\phi \rightarrow K^+K^-$ and $K_S^0 K_L^0$ modes. In the fit, the signal PDF is described by MC-simulated shapes, where the mass and width of X are fixed to LHCb's measurements [25]. The background is composed of $\phi\chi_{c1,c2}$ and a smooth polynomial shape (including both the non- $\gamma\phi J/\psi$ and the continuum $\gamma\phi J/\psi$ contribution). The $\phi\chi_{c1,c2}$ background shapes are from the MC simulation, and their yields are normalized to the cross section measurement described in section 3.2. The contribution for the sum of non- $\gamma\phi J/\psi$ and continuum $\gamma\phi J/\psi$ backgrounds is free. The selection efficiencies and branching fractions of $\phi \rightarrow K^+K^-/K_S^0 K_L^0$ modes are also included in the fit procedure. Figure 8 shows the upper limit of the Born cross section at the 90% C.L. for $e^+e^- \rightarrow \gamma X \rightarrow \gamma\phi J/\psi$ at each c.m. energy, and the numerical results are listed in Tables 9 to 11.

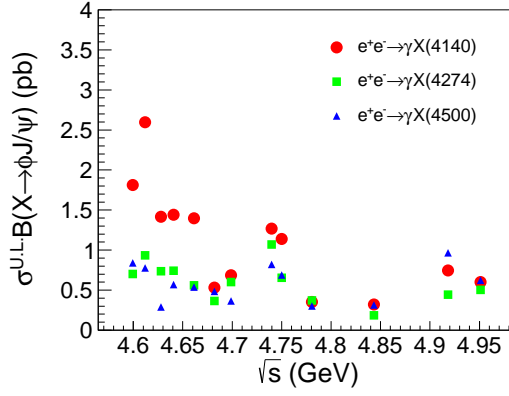


Figure 8. The upper limit of Born cross section product branching fraction at the 90% C.L. versus c.m. energy for $e^+e^- \rightarrow \gamma X(4140)/\gamma X(4274)/\gamma X(4500)$.

\sqrt{s} (GeV)	\mathcal{L}_{int} (pb^{-1})	$\epsilon_{K^+K^-}^3$	$\epsilon_{K^+K^-}^4$	$\epsilon_{K_S^0 K_L^0}$	$\frac{1+\delta}{ 1-\Pi ^2}$	$N_{\gamma X(4140)}^{\text{U.L.}}$	$\sigma^{\text{U.L.}}\mathcal{B}$ (pb)
4.600	586.9	0.214	0.101	0.221	0.91	116.2	1.81
4.612	103.8	0.215	0.097	0.212	0.92	29.8	2.60
4.628	521.5	0.213	0.098	0.212	0.92	81.5	1.42
4.641	552.4	0.213	0.099	0.216	0.92	88.0	1.44
4.661	529.6	0.216	0.101	0.216	0.92	81.7	1.40
4.682	1669.3	0.219	0.101	0.213	0.92	98.0	0.53
4.699	536.5	0.218	0.102	0.213	0.93	41.1	0.69
4.740	164.3	0.213	0.109	0.221	0.93	23.2	1.27
4.750	367.2	0.210	0.107	0.220	0.93	46.6	1.14
4.781	512.8	0.213	0.108	0.219	0.93	20.1	0.35
4.843	527.3	0.213	0.120	0.224	0.94	19.2	0.32
4.918	208.1	0.213	0.122	0.223	0.95	17.7	0.75
4.951	160.4	0.214	0.122	0.218	0.95	11.0	0.60

Table 9. The upper limit of Born cross section at 90% C.L. $\sigma^{\text{U.L.}}\mathcal{B}(X \rightarrow \phi J/\psi)$ for $e^+e^- \rightarrow \gamma X(4140)$ at each c.m. energy \sqrt{s} . The table also includes integrated luminosity \mathcal{L}_{int} , detection efficiency $\epsilon_{K^+K^-}^3$, $\epsilon_{K^+K^-}^4$ and $\epsilon_{K_S^0 K_L^0}$ for the 3-track events in the $\phi \rightarrow K^+K^-$ mode, 4-track events in the $\phi \rightarrow K^+K^-$ mode and the events in the $\phi \rightarrow K_S^0 K_L^0$ mode, respectively, the product of radiative correction factor and vacuum polarization factor $\frac{1+\delta}{|1-\Pi|^2}$, and the 90% C.L. upper limit of the number of fitted events for $\gamma X(4140)$ $N_{\gamma X(4140)}^{\text{U.L.}}$.

\sqrt{s} (GeV)	\mathcal{L}_{int} (pb $^{-1}$)	$\epsilon_{K^+K^-}^3$	$\epsilon_{K^+K^-}^4$	$\epsilon_{K_S^0 K_L^0}$	$\frac{1+\delta}{ 1-\Pi ^2}$	$N_{\gamma X(4274)}^{\text{U.L.}}$	$\sigma^{\text{U.L.}} \mathcal{B}$ (pb)
4.600	586.9	0.217	0.216	0.242	0.88	43.5	0.70
4.612	103.8	0.219	0.211	0.236	0.88	10.3	0.93
4.628	521.5	0.220	0.208	0.230	0.89	41.0	0.74
4.641	552.4	0.221	0.209	0.238	0.89	43.9	0.74
4.661	529.6	0.218	0.207	0.231	0.89	31.6	0.56
4.682	1669.3	0.218	0.209	0.232	0.90	66.0	0.37
4.699	536.5	0.217	0.209	0.232	0.90	34.8	0.60
4.740	164.3	0.221	0.202	0.237	0.91	19.2	1.07
4.750	367.2	0.218	0.208	0.239	0.91	26.3	0.65
4.781	512.8	0.217	0.201	0.239	0.91	20.8	0.37
4.843	527.3	0.220	0.205	0.239	0.92	10.9	0.19
4.918	208.1	0.214	0.205	0.239	0.93	10.3	0.45
4.951	160.4	0.215	0.202	0.232	0.93	9.0	0.50

Table 10. The upper limit of Born cross section at 90% C.L. $\sigma^{\text{U.L.}} \mathcal{B}(X \rightarrow \phi J/\psi)$ for $e^+e^- \rightarrow \gamma X(4274)$ at each c.m. energy \sqrt{s} . The table also includes integrated luminosity \mathcal{L}_{int} , detection efficiency $\epsilon_{K^+K^-}^3$, $\epsilon_{K^+K^-}^4$ and $\epsilon_{K_S^0 K_L^0}$ for the 3-track events in the $\phi \rightarrow K^+K^-$ mode, 4-track events in the $\phi \rightarrow K^+K^-$ mode and the events in the $\phi \rightarrow K_S^0 K_L^0$ mode, respectively, the product of radiative correction factor and vacuum polarization factor $\frac{1+\delta}{|1-\Pi|^2}$ and the 90% C.L. upper limit of the number of fitted events for $\gamma X(4274)$ $N_{\gamma X(4274)}^{\text{U.L.}}$.

\sqrt{s} (GeV)	\mathcal{L}_{int} (pb $^{-1}$)	$\epsilon_{K^+K^-}^3$	$\epsilon_{K^+K^-}^4$	$\epsilon_{K_S^0 K_L^0}$	$\frac{1+\delta}{ 1-\Pi ^2}$	$N_{\gamma X(4500)}^{\text{U.L.}}$	$\sigma^{\text{U.L.}} \mathcal{B}$ (pb)
4.600	586.9	0.181	0.311	0.258	0.82	48.5	0.84
4.612	103.8	0.181	0.303	0.246	0.83	8.0	0.78
4.628	521.5	0.182	0.302	0.244	0.83	15.1	0.29
4.641	552.4	0.180	0.304	0.241	0.84	31.7	0.57
4.661	529.6	0.178	0.303	0.241	0.85	29.1	0.54
4.682	1669.3	0.178	0.296	0.233	0.86	83.7	0.49
4.699	536.5	0.174	0.293	0.236	0.86	20.1	0.36
4.740	164.3	0.169	0.306	0.231	0.87	14.1	0.82
4.750	367.2	0.166	0.305	0.232	0.87	26.4	0.69
4.781	512.8	0.164	0.298	0.231	0.88	16.3	0.30
4.843	527.3	0.164	0.301	0.227	0.89	17.7	0.31
4.918	208.1	0.162	0.299	0.228	0.90	21.7	0.96
4.951	160.4	0.161	0.293	0.223	0.91	10.9	0.62

Table 11. The upper limit of Born cross section at 90% C.L. $\sigma^{\text{U.L.}} \mathcal{B}(X \rightarrow \phi J/\psi)$ for $e^+e^- \rightarrow \gamma X(4500)$ at each c.m. energy \sqrt{s} . The table also includes integrated luminosity \mathcal{L}_{int} , detection efficiency $\epsilon_{K^+K^-}^3$, $\epsilon_{K^+K^-}^4$ and $\epsilon_{K_S^0 K_L^0}$ for the 3-track events in the $\phi \rightarrow K^+K^-$ mode, 4-track events in the $\phi \rightarrow K^+K^-$ mode and the events in the $\phi \rightarrow K_S^0 K_L^0$ mode, respectively, the product of radiative correction factor and vacuum polarization factor $\frac{1+\delta}{|1-\Pi|^2}$ and the 90% C.L. upper limit of the number of fitted events for $\gamma X(4500)$ $N_{\gamma X(4500)}^{\text{U.L.}}$.

4.2 Systematic uncertainty

Since the same selection criteria have been applied to the $e^+e^- \rightarrow \phi\chi_{c1,c2}$ and $e^+e^- \rightarrow \gamma X$ processes, they share most of the systematic uncertainties, such as the tracking efficiency, PID efficiency etc. (cf. section 3.3), and their contributions are listed in Table 12. The systematic uncertainties specifically for the $e^+e^- \rightarrow \gamma X$ process are described below.

The uncertainty due to the signal shape is considered by varying the mass and width of X states within $\pm 1\sigma$, and changing the signal shape to a MC shape convolved with a 2 MeV Gaussian resolution function [58]. For the uncertainty due to background, the number of $\phi\chi_{c1,c2}$ background events is varied within $\pm 1\sigma$, and the smooth polynomial background is studied by varying the order of the polynomial or replacing it with a shape estimated from the sideband data in the fit. The uncertainty associated with the fit range is determined by varying the fit range within ± 10 MeV. By taking these sources into consideration in the fit, the most conservative upper limit for $e^+e^- \rightarrow \gamma X$ is reported.

Source	$\gamma X(4140)$	$\gamma X(4274)$	$\gamma X(4500)$
Luminosity	0.6	0.6	0.6
Tracking	2.5	2.5	2.4
Photon	0.8	0.6	0.5
K_S^0 reconstruction	0.3	0.3	0.3
Kinematic fit	0.6	0.5	0.5
$\mathcal{B}(\phi)$	1.1	1.1	1.1
$\mathcal{B}(J/\psi)$	0.6	0.6	0.6
MUC	1.1	1.1	1.2
Total	3.2	3.1	3.1

Table 12. Systematic uncertainty sources and their contributions (in %) for the cross section of $e^+e^- \rightarrow \gamma X(4140)/\gamma X(4274)/\gamma X(4500)$.

5 Summary

In summary, with 6.4 fb^{-1} of data taken from $\sqrt{s} = 4.600$ to 4.951 GeV, the process of $e^+e^- \rightarrow \gamma\phi J/\psi$ is studied at BESIII. The $e^+e^- \rightarrow \phi\chi_{c1,c2}$ processes with $\chi_{c1,c2} \rightarrow \gamma J/\psi$ are observed with significances over 10σ . The \sqrt{s} -dependent Born cross sections of $e^+e^- \rightarrow \phi\chi_{c1,c2}$ are also measured from 4.600 to 4.951 GeV.

We search for potential vector Y -states in the cross section line shape of $e^+e^- \rightarrow \phi\chi_{c1,c2}$, which might contain $c\bar{c}s\bar{s}$ components in their internal structure. For the $e^+e^- \rightarrow \phi\chi_{c1}$ process, we find no obvious structure in the cross section line shape, and a continuum amplitude can well describe it. For the $e^+e^- \rightarrow \phi\chi_{c2}$ process, there is an enhancement in the cross section line shape. A fit to the cross section with a single BW resonance gives $M = (4672.8 \pm 10.8 \pm 3.9) \text{ MeV}/c^2$ and $\Gamma = (93.2 \pm 19.8 \pm 9.4) \text{ MeV}$ for the mass and width of the structure. The significance of the resonance hypothesis over non-resonance hypothesis is estimated to be 3.1σ . The mass and width of the resonance are consistent with the $Y(4660)$ reported in $e^+e^- \rightarrow \pi^+\pi^-\psi(3686)$ [5–8]. An alternative fit to the cross section with the

coherent sum of a BW and a continuum amplitude gives $M = (4701.8 \pm 10.9 \pm 2.7)$ MeV/ c^2 and $\Gamma = (30.5 \pm 22.3 \pm 14.6)$ MeV for the mass and width of the structure, which has a higher mass and narrower width. The significance for the resonance hypothesis in this model is estimated to be 3.6σ . However, within the current uncertainties, we are not able to distinguish whether it is the same structure as the $Y(4660)$, and the significance for the second fit over the first one is only 2.3σ . This is the first evident structure observed in the $\phi\chi_{c2}$ system.

We also search for a possible X -state in the $\phi J/\psi$ system through the radiative process $e^+e^- \rightarrow \gamma X \rightarrow \gamma\phi J/\psi$. The $\phi J/\psi$ spectrum can be well described by the $\phi\chi_{c1,c2}$ and background events, and no other structure is evident in the $M(\phi J/\psi)$ mass distribution. The $X(4140)$, $X(4274)$ and $X(4500)$ resonances reported by the LHCb Collaboration [25] are not observed, and the upper limits on the Born cross sections for $e^+e^- \rightarrow \gamma X(4140)$, $\gamma X(4274)$, $\gamma X(4500) \rightarrow \gamma\phi J/\psi$ at the 90% C.L. are determined.

Acknowledgments

The BESIII Collaboration thanks the staff of BEPCII and the IHEP computing center for their strong support. This work is supported in part by National Key R&D Program of China under Contracts Nos. 2020YFA0406300, 2020YFA0406400; National Natural Science Foundation of China (NSFC) under Contracts Nos. 11975141, 11635010, 11735014, 11835012, 11935015, 11935016, 11935018, 11961141012, 12022510, 12025502, 12035009, 12035013, 12192260, 12192261, 12192262, 12192263, 12192264, 12192265; the Chinese Academy of Sciences (CAS) Large-Scale Scientific Facility Program; Joint Large-Scale Scientific Facility Funds of the NSFC and CAS under Contract No. U1832207; the CAS Center for Excellence in Particle Physics (CCEPP); 100 Talents Program of CAS; Project ZR2022JQ02 supported by Shandong Provincial Natural Science Foundation; The Institute of Nuclear and Particle Physics (INPAC) and Shanghai Key Laboratory for Particle Physics and Cosmology; ERC under Contract No. 758462; European Union's Horizon 2020 research and innovation programme under Marie Skłodowska-Curie grant agreement under Contract No. 894790; German Research Foundation DFG under Contracts Nos. 443159800, 455635585, Collaborative Research Center CRC 1044, FOR5327, GRK 2149; Istituto Nazionale di Fisica Nucleare, Italy; Ministry of Development of Turkey under Contract No. DPT2006K-120470; National Science and Technology fund; National Science Research and Innovation Fund (NSRF) via the Program Management Unit for Human Resources & Institutional Development, Research and Innovation under Contract No. B16F640076; Olle Engkvist Foundation under Contract No. 200-0605; STFC (United Kingdom); Suranaree University of Technology (SUT), Thailand Science Research and Innovation (TSRI), and National Science Research and Innovation Fund (NSRF) under Contract No. 160355; The Royal Society, UK under Contracts Nos. DH140054, DH160214; The Swedish Research Council; U. S. Department of Energy under Contract No. DE-FG02-05ER41374.

References

- [1] B. Aubert et al. [BaBar Collaboration], *Observation of a broad structure in the $\pi^+\pi^-J/\psi$ mass spectrum around $4.26\text{ GeV}/c^2$* , *Phys. Rev. Lett.* **95** (2005), 142001.
- [2] T. E. Coan et al. [CLEO Collaboration], *Charmonium decays of $Y(4260)$, $\psi(4160)$ and $\psi(4040)$* , *Phys. Rev. Lett.* **96** (2006), 162003.
- [3] C. Z. Yuan et al. [Belle Collaboration], *Measurement of $e^+e^- \rightarrow \pi^+\pi^-J/\psi$ cross section via initial state radiation at Belle*, *Phys. Rev. Lett.* **99** (2007), 182004.
- [4] B. Aubert et al. [BaBar Collaboration], *Evidence of a broad structure at an invariant mass of $4.32\text{ GeV}/c^2$ in the reaction $e^+e^- \rightarrow \pi^+\pi^-\psi(2S)$ measured at BaBar*, *Phys. Rev. Lett.* **98** (2007), 212001.
- [5] X. L. Wang et al. [Belle Collaboration], *Observation of Two Resonant Structures in $e^+e^- \rightarrow \pi^+\pi^-\psi(2S)$ via Initial State Radiation at Belle*, *Phys. Rev. Lett.* **99** (2007), 142002.
- [6] J. P. Lees et al. [BaBar Collaboration], *Study of the reaction $e^+e^- \rightarrow \psi(2S)\pi^+\pi^-$ via initial-state radiation at BaBar*, *Phys. Rev. D* **89** (2014) no.11, 111103.
- [7] X. L. Wang et al. [Belle Collaboration], *Measurement of $e^+e^- \rightarrow \pi^+\pi^-\psi(2S)$ via Initial State Radiation at Belle*, *Phys. Rev. D* **91** (2015), 112007.
- [8] M. Ablikim et al. [BESIII Collaboration], *Cross section measurement of $e^+e^- \rightarrow \pi^+\pi^-(3686)$ from $\sqrt{s}=4.0076$ to 4.6984 GeV* , *Phys. Rev. D* **104** (2021), no.5, 052012.
- [9] W. Kwong, J. L. Rosner and C. Quigg, *Heavy Quark Systems*, *Ann. Rev. Nucl. Part. Sci.* **37** (1987), 325-382.
- [10] P.A. Zyla et al. [Particle Data Group], *Review of Particle Physics*, *PTEP* **2020**, no.8, 083C01 (2020) and 2021 update
- [11] N. Brambilla, S. Eidelman, C. Hanhart, A. Nefediev, C. P. Shen, C. E. Thomas, A. Vairo and C. Z. Yuan, *The XYZ states: experimental and theoretical status and perspectives*, *Phys. Rept.* **873** (2020), 1-154.
- [12] H. X. Chen, W. Chen, X. Liu and S. L. Zhu, *The hidden-charm pentaquark and tetraquark states*, *Phys. Rept.* **639** (2016), 1-121.
- [13] S. Jia et al. [Belle Collaboration], *Observation of a vector charmoniumlike state in $e^+e^- \rightarrow D_s^+D_{s1}(2536)^- + c.c.$* , *Phys. Rev. D* **100** (2019) no.11, 111103.
- [14] S. Jia et al. [Belle Collaboration], *Evidence for a vector charmoniumlike state in $e^+e^- \rightarrow D_s^+D_{s2}^*(2573)^- + c.c.$* , *Phys. Rev. D* **101** (2020) no.9, 091101.
- [15] M. Karliner and J. L. Rosner, *Exotic resonances due to η exchange*, *Nucl. Phys. A* **954** (2016), 365-370.
- [16] J. He, Y. Liu, J. T. Zhu and D. Y. Chen, *$Y(4626)$ as a molecular state from interaction $D_s^*\bar{D}_{s1}(2536) - D_s\bar{D}_{s1}(2536)$* , *Eur. Phys. J. C* **80** (2020) no.3, 246.
- [17] C. Deng, H. Chen and J. Ping, *Can the state $Y(4626)$ be a P-wave tetraquark state $[cs][\bar{c}\bar{s}]?$* , *Phys. Rev. D* **101** (2020) no.5, 054039.
- [18] M. Ablikim et al. [BESIII Collaboration], *Observation of $e^+e^- \rightarrow \phi\chi_{c1}$ and $\phi\chi_{c2}$ at $\sqrt{s}=4.600\text{ GeV}$* , *Phys. Rev. D* **97** (2018) no.3, 032008.
- [19] T. Aaltonen et al. [CDF Collaboration], *Evidence for a Narrow Near-Threshold Structure in the $J/\psi\phi$ Mass Spectrum in $B^+ \rightarrow J/\psi\phi K^+$ Decays*, *Phys. Rev. Lett.* **102** (2009), 242002.

- [20] T. Aaltonen et al. [CDF Collaboration], *Observation of the $Y(4140)$ Structure in the $J/\psi\phi$ Mass Spectrum in $B^\pm \rightarrow J/\psi\phi K^\pm$ Decays*, *Mod. Phys. Lett. A* **32** (2017) no.26, 1750139.
- [21] C. P. Shen [Belle Collaboration], *XYZ particles at Belle*, *Chin. Phys. C* **34** (2010), 615-620.
- [22] R. Aaij et al. [LHCb Collaboration], *Search for the $X(4140)$ state in $B^+ \rightarrow J/\psi\phi K^+$ decays*, *Phys. Rev. D* **85** (2012), 091103.
- [23] R. Aaij et al. [LHCb Collaboration], *Observation of $J/\psi\phi$ structures consistent with exotic states from amplitude analysis of $B^+ \rightarrow J/\psi\phi K^+$ decays*, *Phys. Rev. Lett.* **118** (2017) no.2, 022003.
- [24] R. Aaij et al. [LHCb Collaboration], *Amplitude analysis of $B^+ \rightarrow J/\psi\phi K^+$ decays*, *Phys. Rev. D* **95** (2017) no.1, 012002.
- [25] R. Aaij et al. [LHCb Collaboration], *Observation of New Resonances Decaying to $J/\psi K^+$ and $J/\psi\phi$* , *Phys. Rev. Lett.* **127** (2021) no.8, 082001.
- [26] S. Chatrchyan et al. [CMS Collaboration], *Observation of a Peaking Structure in the $J/\psi\phi$ Mass Spectrum from $B^\pm \rightarrow J/\psi\phi K^\pm$ Decays*, *Phys. Lett. B* **734** (2014), 261-281.
- [27] V. M. Abazov et al. [D0 Collaboration], *A Quasi model independent search for new physics at large transverse momentum*, *Phys. Rev. D* **64** (2001), 012004.
- [28] V. M. Abazov et al. [D0 Collaboration], *Inclusive Production of the $X(4140)$ State in $p\bar{p}$ Collisions at D0*, *Phys. Rev. Lett.* **115** (2015) no.23, 232001.
- [29] J. P. Lees et al. [BaBar Collaboration], *Study of $B^{\pm,0} \rightarrow J/\psi K^+ K^- K^{\pm,0}$ and search for $B^0 \rightarrow J/\psi\phi$ at BABAR*, *Phys. Rev. D* **91** (2015) no.1, 012003.
- [30] M. Ablikim et al. [BESIII Collaboration], *Search for the $Y(4140)$ via $e^+e^- \rightarrow \gamma\phi J/\psi$ at $\sqrt{s}=4.23, 4.26$ and 4.36 GeV*, *Phys. Rev. D* **91** (2015) no.3, 032002.
- [31] D. Ebert, R. N. Faustov and V. O. Galkin, *Excited heavy tetraquarks with hidden charm*, *Eur. Phys. J. C* **58** (2008), 399-405.
- [32] W. Chen and S. L. Zhu, *The Vector and Axial-Vector Charmonium-like States*, *Phys. Rev. D* **83** (2011), 034010.
- [33] Q. F. Lü and Y. B. Dong, *$X(4140)$, $X(4274)$, $X(4500)$, and $X(4700)$ in the relativized quark model*, *Phys. Rev. D* **94** (2016) no.7, 074007.
- [34] J. Wu, Y. R. Liu, K. Chen, X. Liu and S. L. Zhu, *$X(4140)$, $X(4270)$, $X(4500)$ and $X(4700)$ and their $c\bar{s}\bar{c}s$ tetraquark partners*, *Phys. Rev. D* **94** (2016) no.9, 094031.
- [35] Z. G. Wang, *Scalar tetraquark state candidates: $X(3915)$, $X(4500)$ and $X(4700)$* , *Eur. Phys. J. C* **77** (2017) no.2, 78.
- [36] H. X. Chen, E. L. Cui, W. Chen, X. Liu and S. L. Zhu, *Understanding the internal structures of the $X(4140)$, $X(4274)$, $X(4500)$ and $X(4700)$* , *Eur. Phys. J. C* **77** (2017) no.3, 160.
- [37] C. Deng, J. Ping, H. Huang and F. Wang, *Hidden charmed states and multibody color flux-tube dynamics*, *Phys. Rev. D* **98** (2018) no.1, 014026.
- [38] E. Wang, J. J. Xie, L. S. Geng and E. Oset, *The $X(4140)$ and $X(4160)$ resonances in the $e^+e^- \rightarrow \gamma J/\psi\phi$ reaction*, *Chin. Phys. C* **43** (2019) no.11, 113101.
- [39] F. Stancu, *Can $Y(4140)$ be a c anti- c s anti- s tetraquark?*, *J. Phys. G* **37** (2010), 075017. [erratum: *J. Phys. G* **46** (2019) no.1, 019501.]

- [40] X. Liu, H. Huang, J. Ping, D. Chen and X. Zhu, *The explanation of some exotic states in the $c\bar{s}\bar{c}$ tetraquark system*, *Eur. Phys. J. C* **81** (2021) no.10, 950.
- [41] M. Ablikim et al. [BESIII Collaboration], *Measurement of the integrated luminosities at BESIII for data samples at collision energies around 4 GeV*, arXiv:2203.03133 [hep-ex].
- [42] M. Ablikim et al. [BESIII Collaboration], *Luminosities and energies of e^+e^- collision data taken between $\sqrt{s}=4.612$ GeV and 4.946 GeV at BESIII*, arXiv:2205.04809 [hep-ex].
- [43] M. Ablikim et al. [BESIII Collaboration], *Measurement of the center-of-mass energies at BESIII via the di-muon process*, *Chin. Phys. C* **40** (2016) no.6, 063001.
- [44] M. Ablikim et al. [BESIII Collaboration], *Design and Construction of the BESIII Detector*, *Nucl. Instrum. Meth. A* **614** (2010), 345.
- [45] C. H. Yu et al., *BEPCII Performance and Beam Dynamics Studies on Luminosity*, Proceedings of IPAC2016, Busan, Korea, 2016, doi:10.18429/JACoW-IPAC2016-TUYA01.
- [46] M. Ablikim et al. [BESIII Collaboration], *White Paper on the Future Physics Programme of BESIII*, *Chin. Phys. C* **44** (2020), 040001.
- [47] X. Li et al., *Study of MRPC technology for BESIII endcap-TOF upgrade*, *Radiat. Detect. Technol. Methods* **1** (2017), 13; Y. X. Guo et al., *The study of time calibration for upgraded end cap TOF of BESIII*, *Radiat. Detect. Technol. Methods* **1** (2017), 15; P. Cao et al., *Design and construction of the new BESIII endcap Time-of-Flight system with MRPC Technology*, *Nucl. Instrum. Meth. A* **953** (2020), 163053.
- [48] S. Agostinelli et al. [GEANT4 Collaboration], *GEANT4: A Simulation toolkit*, *Nucl. Instrum. Meth. A* **506** (2003), 250.
- [49] S. Jadach, B. F. L. Ward and Z. Was, *Coherent exclusive exponentiation for precision Monte Carlo calculations*, *Phys. Rev. D* **63** (2001), 113009; *Comput. Phys. Commun.* **130** (2000), 260.
- [50] D. J. Lange, *The EvtGen particle decay simulation package*, *Nucl. Instrum. Meth. A* **462** (2001), 152; R. G. Ping, *Event generators at BESIII*, *Chin. Phys. C* **32** (2008), 599.
- [51] J. C. Chen, G. S. Huang, X. R. Qi, D. H. Zhang and Y. S. Zhu, *Event generator for J/ψ and $\psi(2S)$ decay*, *Phys. Rev. D* **62** (2000), 034003; R. L. Yang, R. G. Ping and H. Chen, *Tuning and Validation of the Lundcharm Model with J/ψ Decays*, *Chin. Phys. Lett.* **31** (2014), 061301.
- [52] E. Richter-Was, *QED bremsstrahlung in semileptonic B and leptonic tau decays*, *Phys. Lett. B* **303** (1993), 163.
- [53] S. Actis et al. [Working Group on Radiative Corrections and Monte Carlo Generators for Low Energies], *Quest for precision in hadronic cross sections at low energy: Monte Carlo tools vs. experimental data*, *Eur. Phys. J. C* **66** (2010), 585-686.
- [54] M. Ablikim et al. [BESIII Collaboration], *Precise measurement of the $e^+e^- \rightarrow \pi^+\pi^- J/\psi$ cross section at center-of-mass energies from 3.77 to 4.60 GeV*, *Phys. Rev. Lett.* **118** (2017) no.9, 092001.
- [55] M. Ablikim et al. [BESIII Collaboration], *Study of decay dynamics and CP asymmetry in $D^+ \rightarrow K_L^0 e^+ \nu_e$ decay*, *Phys. Rev. D* **92** (2015) no.11, 112008.
- [56] M. Ablikim et al. [BESIII Collaboration], *Branching fraction measurements of χ_{c0} and χ_{c2} to $\pi^0\pi^0$ and $\eta\eta$* , *Phys. Rev. D* **81** (2010), 052005.

- [57] M. Ablikim et al. [BESIII Collaboration], *Search for hadronic transition $\chi_{cJ} \rightarrow \eta_c \pi^+ \pi^-$ and observation of $\chi_{cJ} \rightarrow K \bar{K} \pi \pi$* , *Phys. Rev. D* **87** (2013) no.1, 012002.
- [58] M. Ablikim et al. [BESIII Collaboration], *Observation of $e^+e^- \rightarrow \gamma X(3872)$ at BESIII*,” *Phys. Rev. Lett.* **112** (2014) no.9, 092001.

A Fit result for $M(\gamma J/\psi)$

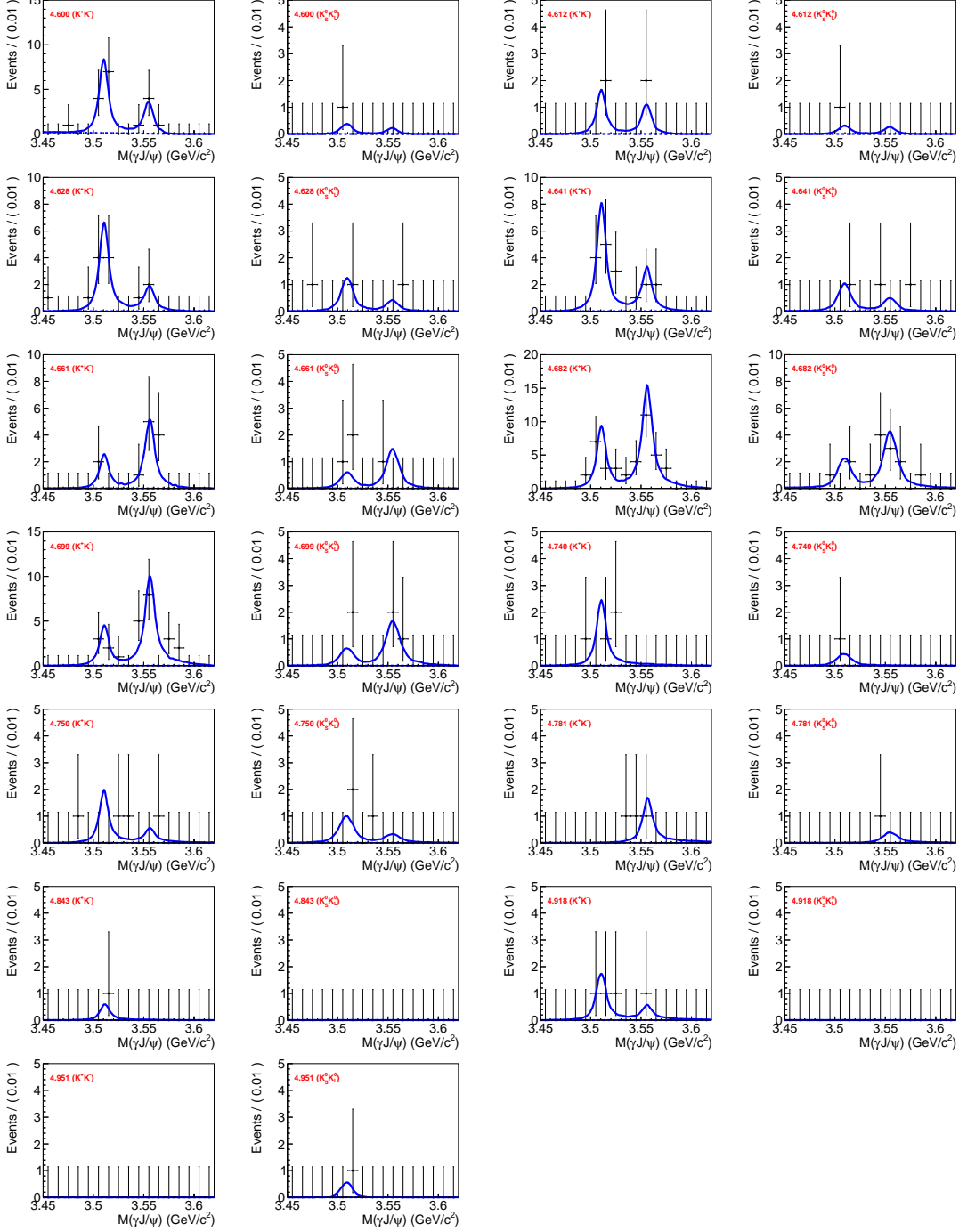


Figure 9. The simultaneous fit to $M(\gamma J/\psi)$ for $\phi \rightarrow K^+K^-$ and $\phi \rightarrow K_S^0 K_L^0$ modes from 4.600 to 4.951 GeV. Dots with error bars are data, blue lines are the fit results.

B Systematic uncertainty in cross section measurement

Source	4.600	4.612	4.628	4.641	4.661	4.682	4.699	4.740	4.750	4.781	4.843	4.918	4.951
Luminosity	0.60	0.60	0.60	0.60	0.60	0.60	0.60	0.60	0.60	0.60	0.60	0.60	0.60
Tracking	2.47	2.46	2.45	2.44	2.42	2.42	2.41	2.40	2.40	2.40	2.39	2.39	2.38
Photon	0.80	0.78	0.75	0.73	0.68	0.65	0.62	0.57	0.57	0.54	0.50	0.48	0.46
K_S^0	0.28	0.28	0.27	0.26	0.25	0.25	0.25	0.24	0.24	0.24	0.23	0.23	0.23
Kinematic fit	0.54	0.53	0.52	0.52	0.50	0.49	0.48	0.46	0.46	0.45	0.44	0.43	0.43
$\mathcal{B}(\phi)$	0.81	0.82	0.82	0.82	0.83	0.83	0.83	0.84	0.83	0.84	0.84	0.84	0.84
$\mathcal{B}(\chi_{c1})$	2.90	2.90	2.90	2.90	2.90	2.90	2.90	2.90	2.90	2.90	2.90	2.90	2.90
$\mathcal{B}(J/\psi)$	0.60	0.60	0.60	0.60	0.60	0.60	0.60	0.60	0.60	0.60	0.60	0.60	0.60
Radiative correction	3.16	2.48	1.62	1.90	1.42	0.40	0.49	0.57	0.70	1.60	1.18	2.46	1.37
MC model	0.30	0.46	0.21	0.23	0.10	0.18	0.28	0.48	0.43	0.57	0.49	0.48	0.51
Muon hit depth	1.51	0.87	1.15	1.09	1.06	0.86	0.92	0.97	1.44	1.28	1.39	0.95	1.34
Fit related	5.54	5.54	5.54	5.54	5.54	5.54	5.54	5.54	5.54	5.54	5.54	5.54	5.54
Total	7.75	7.39	7.17	7.22	7.09	6.93	6.94	6.96	7.04	7.16	7.09	7.34	7.11

Table 13. The systematic uncertainties (in %) for $e^+e^- \rightarrow \phi\chi_{c1}$ cross sections at each energy point.

Source	4.600	4.612	4.628	4.641	4.661	4.682	4.699	4.740	4.750	4.781	4.843	4.918	4.951
Luminosity	0.60	0.60	0.60	0.60	0.60	0.60	0.60	0.60	0.60	0.60	0.60	0.60	0.60
Tracking	2.55	2.50	2.49	2.47	2.46	2.44	2.44	2.42	2.42	2.42	2.40	2.40	2.40
Photon	0.92	0.88	0.84	0.81	0.77	0.73	0.70	0.64	0.63	0.59	0.54	0.50	0.49
K_S^0	0.33	0.30	0.29	0.28	0.27	0.27	0.26	0.25	0.25	0.25	0.24	0.24	0.24
Kinematic fit	0.58	0.57	0.55	0.54	0.53	0.52	0.51	0.49	0.48	0.47	0.45	0.44	0.44
$\mathcal{B}(\phi)$	0.80	0.81	0.81	0.81	0.82	0.82	0.82	0.83	0.83	0.83	0.83	0.83	0.84
$\mathcal{B}(\chi_{c2})$	2.60	2.60	2.60	2.60	2.60	2.60	2.60	2.60	2.60	2.60	2.60	2.60	2.60
$\mathcal{B}(J/\psi)$	0.60	0.60	0.60	0.60	0.60	0.60	0.60	0.60	0.60	0.60	0.60	0.60	0.60
Radiative correction	5.17	7.42	6.23	6.57	3.27	5.31	10.57	17.33	15.53	5.61	1.28	0.69	2.93
MC model	0.38	0.43	0.37	0.38	0.27	0.16	0.11	0.24	0.34	0.39	0.47	0.51	0.44
Muon hit depth	1.45	0.85	1.12	1.08	1.05	0.85	0.91	0.96	1.43	1.26	1.37	0.95	1.33
Fit related	7.14	7.14	7.14	7.14	7.14	7.14	7.14	7.14	7.14	7.14	7.14	7.14	7.14
Total	9.79	11.07	10.33	10.53	8.83	9.74	13.36	19.16	17.58	9.94	8.32	8.19	8.72

Table 14. The systematic uncertainties (in %) for $e^+e^- \rightarrow \phi\chi_{c2}$ cross sections at each energy point.